NONAXISYMMETRIC INSTABILITIES OF SELF-GRAVITATING DISKS. *I* TOROIDS

Kathryn Hadley & James N. Imamura
Institute of Theoretical Science and Department of Physics, University of Oregon, Eugene, OR 97403

ABSTRACT

We investigate the properties of the nonaxisymmetric disk modes commonly referred to as P, I, and J modes in self-gravitating polytropic toroids with power law angular velocity distributions. We consider modes with azimuthal dependence $e^{im\phi}$, where m is an integer and ϕ is the azimuthal angle. We find that instability sets in through $m = 2$ barlike I modes at $T/|W| \sim 0.16$-0.18 depending upon the chosen angular velocity law, where T is the rotational kinetic energy and W is the gravitational energy of the toroid. Instability in the $m = 2$ barlike I mode peaks in strength around $T/|W| = 0.22$-0.23 after which it weakens, eventually stabilizing around $T/|W| \sim 0.25$-0.26. One-armed spiral modes ($m = 1$ modes) become unstable around $T/|W| = 0.19$ eventually dominating the barlike I mode when $T/|W| \gtrsim 0.25$. However, almost immediately after the $m = 1$ mode overtakes the barlike I mode, higher-m J modes appear. J modes with $m = 2$, 3, and 4 become unstable for $T/|W| \gtrsim 0.25$-0.26, 0.23-0.25, and 0.25-0.26, respectively. $m \geq 3$ J modes dominate the $m = 1$ mode for $T/|W| \gtrsim 0.27$. As $T/|W|$ increases, nonaxisymmetric instability sets in through higher and higher m modes. Neither I mode nor J mode instabilities produce prompt fission in toroids in the nonlinear regime.

Subject headings: Hydrodynamics: Stability; Stars: Rotation

1. INTRODUCTION

Self-gravitating toroids and disks arise in a wide range of astrophysical environments playing crucial roles in the evolution of systems on galactic to stellar scales. The nature and stability properties of self-gravitating toroids and disks are not, hoverer, completely understood. Extensive work on infinitesimally thin accretion disks and self-gravitating annuli has been performed. Much less attention has been directed toward thick self-gravitating toroids and disks. Cold (thin) disks which, essentially, are two-dimensional (2D), are known to exhibit a rich spectrum of modes (*e.g.,* Lin & Papaloizou 1995). It is not clear how much of the 2D work carries over to hot (thick) disks (toroids), however, the extra degree-of-freedom in hot disks may introduce new types of modes as well as simply affecting the properties of 2D modes. Here, we begin an investigation of the

nonaxisymmetric instabilities of thick, three-dimensional (3D) self-gravitating disks and toroids. In this paper, we consider self-gravitating toroids. In later works we study star/disk systems where the central star is treated as a point mass and then cases where it is resolved, allowing us to model the coupling of internal modes excited in the star with nonaxisymmetric modes excited in the disk.

Self-gravitating toroids have been the subject of a handful of studies over the years (Wong 1974; Eriguchi & Hachisu 1983; Hachisu & Eriguchi 1985; Hachisu, Tohline, & Eriguchi 1987, 1988; Tohline & Hachisu 1990; Woodward, Tohline & Hachisu 1994). The earliest workers examined the properties of incompressible fluid toroids (cf. Wong 1974; Eriguchi & Hachisu 1983 and references therein). They showed that a ring-like sequence branched off the Maclaurin sequence with increasing angular momentum at $T/|W| = 0.451$, the one-ring sequence (Hachisu & Eriguchi 1985). Similar to the behavior shown by Maclaurin spheroids, it was found for spheroids with polytropic equations of state and angular momentum distributions characteristic of Maclaurin spheroids, that ring-like sequences branched-off Maclaurin-like polytropic sequences at $T/|W| \sim 0.41$. Surprisingly, however, it was found in cloud collapse simulations that ring-like structures appeared at $T/|W| \sim 0.39$, not $T/|W| \sim 0.41$. This discrepancy was resolved when it was shown that although ring-like objects did indeed bifurcate from Maclaurin-like sequences at $T/|W| \sim 0.41$, these sequences were double-valued in $T/|W|$ at lower angular momentum j. Ring-like equilibria were possible for smaller j where Maclaurin-like spheroids had $T/|W| \sim 0.39$. As j increased, two ring-like branches formed with the upper branch connecting to the Maclaurin-like sequence at $T/|W| = 0.41$. Collapsing clouds made the transition to ring-like equilibria at the minimum in $T/|W|$ and then proceeded to evolve along the lower of the two ring-like sequences (Hachisu, Tohline, & Eriguchi 1987, 1988). Despite the smaller $T/|W|$ threshold for the transition to ring-like structures for both compressible and incompressible spheroids, rings (toroids) still appear well after $T/|W| = 0.27$ is passed, the stability limit for bar modes in Maclaurin spheroids and barlike modes in rotating Maclaurin-like polytropes (Tassoul 1978). Toroids with Maclaurin-like angular momentum distributions are thus likely to be strongly unstable and not viable steps in the secular evolution of a collapsing interstellar cloud. They may, however, represent metastable states reached during inviscid axisymmetric dynamical collapses. Not as cleanly connected to the collapse problem but perhaps more useful from a theoretical standpoint and observational viewpoint, are polytropic toroids with power law angular velocity distributions, $\Omega(\varpi) \propto \varpi^{-q}$ (*e.g.*, Tohline 2002). Such toroids may arise after instabilities and viscosity have acted and in fact may be more likely to exist in nature than Maclaurin-like toroids because for a broad range of q, stable toroids exist to zero angular momentum unlike toroids with the Maclaurin spheroid angular momentum distribution for which equilibria exist only at high angular momenta.

Self-gravitating polytropic toroids with power law angular velocity distributions $\Omega(\varpi)$ were investigated by Hachisu, Tohline, & Eriguchi (1987,1988), Tohline & Hachisu (1990) and Woodward, Tohline, & Hachisu (1994). Hachisu, Tohline, & Eriguchi (1987,1988) argued that instability in self-gravitating toroids could set in as early as $T/|W| = 0.142$, based on time scale

arguments. Tohline & Hachisu (1990). Woodward, Tohline, & Hachisu (1994), using nonlinear hydrodynamics, showed that barlike dynamic instabilities set in as early as $T/|W| = 0.17$ in polytropic toroids. In their pioneering works, Tohline & Hachisu (1990) and Woodward, Tohline, & Hachisu (1994) considered only a handful of models to cover the extensive parameter space occupied by self-gravitating, rotating toroids defined by the compressibility of the toroid, the angular velocity distribution of the toroid, and the angular momentum content of the toroid. A broader search of the parameter space is needed to elucidate the properties of the various nonaxisymmetric modes of self-gravitating toroids. In this paper we consider axisymmetric equilibrium toroids and so investigate the properties of nonaxisymmetric modes with azimuthal dependence given by $e^{im\phi}$ where m is the azimuthal mode number and ϕ is the azimuthal angular coordinate. We determine the properties of the fastest growing nonaxisymmetric modes in unstable equilibrium models for given m and then compare and contrast the nonaxisymmetric modes that arise in toroidal structures to those that arise in spheroidal polytropic stars (*cf.*, Toman *et al.* 1998, Imamura *et al.* 2000), and to the nonaxisymmetric modes isolated in incompressible narrow toroids (ICTs) (*e.g.,* Andalib, Tohline, & Christodoulou 1997) and in polytropic toroids (Tohline & Hachisu 1990, Woodward, Tohline, & Hachisu 1994). We pay particular attention to ICTs around low-mass stars because the parameter space accessible to incompressible narrow toroids (ICTs) with constant specific angular momentum distribution has been thoroughly explored, *e.g.,* see Andalib, Tohline, & Christodoulou (1997). The stability properties for toroids over their larger parameter space are not well-studied. Tohline & Hachisu (1990) and Woodward, Tohline, & Hachisu (1994) investigated the stability properties of the even m modes for seven toroids with $n = 3/2$ for $q = 3/2$, $7/4$, and 2. We extend and expand upon these works through an extensive exploration of parameter space for self-gravitating toroids in which we consider both even m and odd m modes. For selected toroids, we also follow the development of instability from the linear regime, through the quasi-linear regime, and into the fully nonlinear regime.

The remainder of our paper is organized as follows. In §2, we present and then discuss the properties of the equilibrium toroids. In §3, we discuss the nonaxisymmetric modes of toroids and disks and we describe the methods we use to model nonaxisymmetric modes in toroids. In §4, we present our numerical results. In §5, we compare our results to previous works and then discuss our results in the context of star formation. Finally in §6, we summarize our results and conclusions.

2. EQUILIBRIUM TOROID MODELS

The inviscid hydrodynamics equations for an isentropic gas are

$$0 = \frac{\partial \rho}{\partial t} + \nabla \cdot (\rho \mathbf{v}), \tag{1}$$

$$0 = \rho \left(\frac{\partial}{\partial t} + \mathbf{v} \cdot \nabla \right) \mathbf{v} + \nabla P + \rho \nabla \Phi_g, \tag{2}$$

$$0 \quad = \quad \left(\frac{\partial}{\partial t} + \mathbf{v} \cdot \nabla\right) (P\rho^{-\gamma}) \tag{3}$$

where t is time, ρ is the density, $\mathbf{v}$ is the velocity, P is the pressure, Φ_g is the gravitational potential, and γ is the adiabatic index. In steady-state, we drop the time derivatives and assume axisymmetry. For an isentropic gas, the polytropic pressure-density relationship, $P(\rho) = K\rho^{\gamma}$ where K is the polytropic constant, $\gamma = 1 + 1/n$, and n is the polytropic index is valid. The velocity field is taken to have power law angular velocity distribution $\Omega(\varpi) = \Omega_{\circ}(\varpi/R_{max})^{-q}$, where $\Omega_{\circ}$ is a normalization constant, R_{max} is the radius of the maximum density, ϖ is the cylindrical radial coordinate, and q is a constant. We consider toroids with $n = 3/2$ and $q = 1$, $3/2$, and 2. The equations are solved on cylindrical grids with uniformly spaced cells and typical dimension $n_{\varpi} \times n_z = 512 \times 512$. We use a Hachisu-type (Hachisu 1986) self-consistent field code to calculate equilibrium structures (Pickett, Durisen, & Davis 1996).

Families of toroids are defined by (n, q)-pairs. Individual family members are parametrized by the ratio of the radius of the inner edge of the toroid R_{-} to the radius of the outer edge of the toroid R_{+}. There is a one-to-one correspondence between the ratio R_{-}/R_{+} and $T/|W|$ (and the angular momentum j) for toroids with power law $\Omega(\varpi)$ distributions. For large R_{-}/R_{+}, toroids are more symmetric with cross-sections approaching circular in shape. Properties of the equilibrium toroids are summarized in Tables 1, 2, & 3. In the far right column is listed $\epsilon = (R_{max} - R_{-})/R_{max}$, a measure of the width of the toroid. Here, R_{max} is the location of the maximum density in the toroid. For toroids with small $T/|W|$ (small R_{-}/R_{+}), $\epsilon \rightarrow 1$. For toroids with large $T/|W|$ (large R_{-}/R_{+}), $\epsilon \rightarrow 0$. ICT approximations are most accurate when $\epsilon \ll 1$. Unless otherwise noted, all quantities are presented in polytrope units, the unit system where $G = K = M = 1$. Quantities in polytrope units may be converted to physical units using the transformations given in Williams & Tohline (1987). More extensive compilations of the properties of polytropic toroids may be found in Hachisu, Tohline, & Eriguchi (1987, 1988).

Equilibrium toroids have several characteristic radii important for understanding the nature of their eigenmodes (*e.g.,* Papaloizou & Savonije 1991). Among these are: (a) the location of the density maximum of the toroid R_{max}; (b) the location of the extremum of the vortensity distribution R_{λ} where the vortensity λ is defined as the mass column density Σ divided by the local vorticity. For rotation on cylinders and power law $\Omega(\varpi)$, the vortensity

$$\lambda = \left(\frac{\Sigma}{(2-q)\Omega}\right) \hat{\mathbf{z}}. \tag{4}$$

(c) The boundaries of the region where the Toomre Q-parameter

$$\mathrm{Q} = \frac{c_s \kappa}{\pi \mathrm{G} \Sigma} \tag{5}$$

drops below one. Here, c_s is the sound speed, κ is the epicyclic frequency (see Equation [44]) and Σ is the surface density. Q reaches maxima at the inner and outer edges of the toroid with minimum near the density maximum. Local axisymmetric modes may be unstable where $Q \lesssim 1$ and nonaxisymmetric modes unstable when $Q \gtrsim 1$ (*e.g.*, Papaloizou & Lin 1995).

3. NONAXISYMMETRIC INSTABILITIES IN TOROIDS

3.1. Nonaxisymmetric Disk Modes

Self-gravitating disks are susceptible to nonaxisymmetric instability though several modes. We consider the self-gravitating I and J modes, and the shear-driven P modes (*e.g.,* see Andalib, Tohline, & Christodoulou 1997). (i) P modes were discovered by Papaloizou & Pringle (1984) in studies of non-self-gravitating disks. They are driven by the coupling of edge waves across an evanescent wave region around corotation. For P modes, corotation falls at or near the location of the density maximum ρ_{max} in the disk. Later workers showed that although P modes can persist into the self-gravitating regime, they weaken greatly in strength with increasing self-gravity. We do not find P modes in rapidly rotating self-gravitating toroids. (ii) I modes (intermediate modes) arise only in self-gravitating disks. They are driven by the merger of two waves which carry equal but opposite amounts of angular momentum. One wave is driven by self-gravity and represents azimuthal compressions, the other wave is driven by free epicyclic motions. Corotation for I modes falls well outside the location of ρ_{max} in the disk. (iii) J modes also appear only in self-gravitating disks. They also result from the merger of two waves, however, both waves are driven by self-gravity. J modes are related to Jeans instabilities. Corotation for J modes falls near the location of ρ_{max}. (iv) For ICTs, it was found that instability in I modes sets in well before instability in J modes systems with given star mass to disk mass ratio, M_*/M_d.

3.2. Numerical Modeling of Nonaxisymmetric Disk Modes

We find the fastest growing mode for given m in the linear regime by solving an initial value problem (IVP) in which the evolution of random, low amplitude, Eulerian perturbations are followed away from equilibrium in unstable toroidal configurations. The IVP equations are found from linearization of the hydrodynamics equations (Equations [1]-[3]) using Eulerian perturbations of the form

$$\rho = \rho_o + \delta\rho(\varpi, z, t)e^{im\phi}, \tag{6}$$

$$v_\varpi = \delta v_\varpi(\varpi, z, t)e^{im\phi}, \tag{7}$$

$$v_\phi = \Omega\varpi + \delta v_\phi(\varpi, z, t)e^{im\phi}, \tag{8}$$

$$v_z = \delta v_z(\varpi, z, t)e^{im\phi}, \tag{9}$$

where ρ_o and Ω are the equilibrium density and angular velocity, respectively. The linearized hydrodynamic equations are then

$$\frac{\partial\delta\rho}{\partial t} = -im\Omega\delta\rho - \rho_o\frac{\delta v_\varpi}{\varpi} - \delta v_\varpi\frac{\partial\rho_o}{\partial\varpi} - \delta v_z\frac{\partial\rho_o}{\partial z} - \rho_o\left(\frac{\partial\delta v_\varpi}{\partial\varpi} + \frac{im}{\varpi}\delta v_\phi + \frac{\partial\delta v_z}{\partial z}\right) \tag{10}$$

$$\frac{\partial\delta v_\varpi}{\partial t} = -im\Omega\delta v_\varpi + 2\Omega\delta v_\phi - \frac{\gamma P_o}{\rho_o^2}\frac{\partial\delta\rho}{\partial\varpi} - (\gamma-2)\frac{\delta\rho}{\rho_o^2}\frac{\partial P_o}{\partial\varpi} - \frac{\partial\delta\Phi}{\partial\varpi}, \tag{11}$$

$$\frac{\partial \delta v_\phi}{\partial t} = -im\Omega\delta v_\phi - \frac{\delta v_\varpi}{\varpi}\frac{\partial(\Omega\varpi^2)}{\partial\varpi} - \frac{im}{\varpi}\frac{\gamma P_o}{\rho_o^2}\delta\rho - \frac{im}{\varpi}\delta\Phi, \tag{12}$$

and

$$\frac{\partial \delta v_z}{\partial t} = -im\Omega\delta v_z - \frac{\gamma P_o}{\rho_o^2}\frac{\partial\delta\rho}{\partial z} - (\gamma-2)\frac{\delta\rho}{\rho_o^2}\frac{\partial P_o}{\partial z} - \frac{\partial\delta\Phi}{\partial z}. \tag{13}$$

In the above, we suppressed the "(ϖ, z, t)" from the notation describing the perturbations, and we let $P_o = K\rho_o^\gamma$. The linearized equations are complex. We solve them as pairs of real equations by adopting the representations,

$$\delta\rho = \eta_R + i\eta_I, \tag{14}$$
$$\delta v_\varpi = T_R + iT_I, \tag{15}$$
$$\delta v_\phi = V_R + iV_I, \tag{16}$$
$$\delta v_z = W_R + iW_I, \tag{17}$$
$$\delta\Phi = \Phi_R + i\Phi_I \tag{18}$$

which are then substituted into the linearized equations. We find

$$\frac{\partial\eta_R}{\partial t} = m\Omega\eta_I - T_R\frac{\rho_o}{\varpi}\left(1+\frac{\varpi}{\rho_o}\frac{\partial\rho_o}{\partial\varpi}\right) - W_R\frac{\partial\rho_o}{\partial z} - \rho_o\left(\frac{\partial T_R}{\partial\varpi} - \frac{m}{\varpi}V_I + \frac{\partial W_R}{\partial z}\right), \tag{19}$$
$$\frac{\partial\eta_I}{\partial t} = -m\Omega\eta_R - T_I\frac{\rho_o}{\varpi}\left(1+\frac{\varpi}{\rho_o}\frac{\partial\rho_o}{\partial\varpi}\right) - W_I\frac{\partial\rho_o}{\partial z} - \rho_o\left(\frac{\partial T_I}{\partial\varpi} + \frac{m}{\varpi}V_R + \frac{\partial W_I}{\partial z}\right), \tag{20}$$
$$\frac{\partial T_R}{\partial t} = m\Omega T_I + 2\Omega V_R - \gamma\frac{P_o}{\rho_o^2}\frac{\partial\eta_R}{\partial\varpi} - (\gamma-2)\frac{\eta_R}{\rho_o^2}\frac{\partial P_o}{\partial\varpi} - \frac{\partial\Phi_R}{\partial\varpi}, \tag{21}$$
$$\frac{\partial T_I}{\partial t} = -m\Omega T_R + 2\Omega V_I - \gamma\frac{P_o}{\rho_o^2}\frac{\partial\eta_I}{\partial\varpi} - (\gamma-2)\frac{\eta_I}{\rho_o^2}\frac{\partial P_o}{\partial\varpi} - \frac{\partial\Phi_I}{\partial\varpi}, \tag{22}$$
$$\frac{\partial V_R}{\partial t} = m\Omega V_I - \frac{T_R}{\varpi}\frac{\partial(\Omega\varpi^2)}{\partial\varpi} + \frac{m}{\varpi}\left(\frac{\gamma P_o}{\rho_o^2}\eta_I + \Phi_I\right), \tag{23}$$
$$\frac{\partial V_I}{\partial t} = -m\Omega V_R - \frac{T_I}{\varpi}\frac{\partial(\Omega\varpi^2)}{\partial\varpi} - \frac{m}{\varpi}\left(\frac{\gamma P_o}{\rho_o^2}\eta_R + \Phi_R\right), \tag{24}$$
$$\frac{\partial W_R}{\partial t} = m\Omega W_I - \frac{\gamma P_o}{\rho_o^2}\frac{\partial\eta_R}{\partial z} - (\gamma-2)\frac{\eta_R}{\rho_o^2}\frac{\partial P_o}{\partial z} - \frac{\partial\Phi_R}{\partial z}, \tag{25}$$

and

$$\frac{\partial W_I}{\partial t} = -m\Omega W_R - \frac{\gamma P_o}{\rho_o^2}\frac{\partial\eta_I}{\partial z} - (\gamma-2)\frac{\eta_I}{\rho_o^2}\frac{\partial P_o}{\partial z} - \frac{\partial\Phi_I}{\partial z}. \tag{26}$$

The gravitational perturbation is found from solution of the Poisson equation,

$$\nabla^2\delta\Phi = 4\pi G\delta\rho, \tag{27}$$

and Φ_R and Φ_I may be calculated from η_R and η_I, individually. To calculate Φ_R and Φ_I, we use a Poisson equation solver taken from the numerical hydrodynamics code of Pickett, Durisen, & Davis

(1996). The IVP equations are discretized on a computational grid which divides (ϖ,z)-space into uniformly sized cells. Densities are defined at cell centers and the velocities at cell vertices. The equations are solved at cell centers by approximating the spatial derivatives with finite differences while leaving the time derivatives continuous. This leads to a set of coupled evolution equations in the time, t. The system of coupled equations is advanced in time using a Runge-Kutta algorithm. Simulations are performed on the same grids as used for the equilibrium calculations. We impose the following boundary conditions: (1) the perturbations are forced to be symmetric about the equatorial plane; (2) the perturbed radial and azimuthal velocities are set to 0 on the rotation axis; (3) the density perturbation is unconstrained and the velocity perturbations are set to 0 on the surface of the unperturbed polytrope. (4) Continuity of the gravitational potential at the surface of the polytrope is guaranteed by imposing boundary conditions on the potential on the surface of the cylinder defined by the maximum ϖ and z of the computational grid. The potential on the surface of the cylinder is found by solving the integral form for the perturbed gravitational potential.

Exponentially growing global modes are identified as follows. We first plot the phase and logarithm of the amplitude of the relative density perturbation at three locations in the equatorial plane of the toroid. If the perturbation settles into the same pattern of growth at the three radii, we start to monitor the full structure of the disturbance to determine if the toroid has fallen into global growth. After growth is global and uniform, the growth rate for the mode is determined by a least squares fit to the exponential growth portion of the evolution and the oscillation frequency for the mode found by a least squares fit to the linear portion of the phase evolution. Models are considered stable if coherent modes do not develop within 30 to 50 τ_{max}, where τ_{max} is the disk rotation period at the location of the density maximum (see Table 1).

Early nonlinear evolution of unstable barlike modes in polytropes is dominated by angular momentum transport which arises from a gravitational self-interaction torque between the forming central bar and *ejected* spiral arms (Imamura, Pickett, & Durisen 2001). Imamura, Pickett, & Durisen explicitly demonstrated that this interaction limited the growth of barlike modes in polytropes using a quasi-linear (QL) formulation for the torque. The time-averaged, QL self-interaction torque on an annulus between ϖ and $\varpi + \mathrm{d}\varpi$ is

$$\gamma = -m\pi \int |\delta\rho||\delta\Phi| \sin(\phi_\rho - \phi_\Phi)\mathrm{dz} \tag{28}$$

where $\delta\rho$ and $\delta\Phi$ are the perturbed density and gravitational potential, and ϕ_ρ and ϕ_Φ are the phases of the density and gravitational perturbations (Imamura, Pickett, & Durisen 2001). The QL torque determines the size and properties of the bars which form and how the angular momentum j is redistributed in the nonlinear development of the bar mode instability in polytropes, features which allowed Imamura, Durisen, & Pickett (2001) to predict the initial development of the $m = 2$ barlike mode in the nonlinear regime based only on the linear eigenfunctions. We apply the QL theory to toroids when they are weakly nonlinear.

Nonlinear development of nonaxisymmetric modes in selected toroids is followed using the

three-dimensional (3D) hydrodynamics computer code described in Pickett, Durisen, & Davis (1996). Our numerical hydrodynamics code solves equations (1) to (3) using an explicit TVD transport scheme which is second-order in space and time. The equations are solved on a uniform cylindrical grid chosen to match that used in the equilibrium numerical code. Consequently, equilibrium models as described in §2.1 can be input directly into the nonlinear hydrodynamics computer code. The stability analysis is performed by perturbing the equilibrium density distribution with a random perturbation. We set

$$\rho(\mathbf{r}, t = 0) = \rho_\circ(\mathbf{r})(1 + \epsilon[1 - 2\mathcal{R}(\mathbf{r})]) \tag{29}$$

where $\rho(\mathbf{r}, t)$ is the density, $\rho_\circ(\mathbf{r})$ is the equilibrium density, $\mathcal{R}(\mathbf{r})$ is a random number which ranges between 0 and 1, and ϵ is a small parameter set to 10^{-6}. Boundary conditions on the grid are outflow at the largest r and z, and reflection through the equatorial plane. The gravitational potential Φ_g is found by direct solution of the Poisson equation. Boundary conditions are determined using an expansion for Φ_g in spherical harmonics keeping terms up to $\ell = m = 10$. As the bar mode develops and the toroid expands, the grid is enlarged when necessary. The maximum grid size used is (512,128,128).

3.3. Energy and Work Integrals

The perturbed energy equation is given by

$$\frac{\partial \langle \mathcal{E} \rangle}{\partial t} = \sigma_R + \sigma_\Pi + \sigma_\Phi \tag{30}$$

where $\langle \mathcal{E} \rangle$, the energy of the mode, is composed of the perturbed kinetic and acoustic energies

$$\langle \mathcal{E} \rangle = 0.5\ \rho_\circ \langle \delta v \cdot \delta v \rangle + 0.5\gamma(P_\circ/\rho_\circ^2) \langle \delta\rho \rangle^2 \tag{31}$$

(*e.g.,* see Kojima 1989). In the above, quantities enclosed in brackets, $\langle \mathrm{X} \rangle$, indicate the time-average of X, the enclosed quantity, and the terms σ_R, σ_Φ, and σ_Π are defined as follows. σ_R is the Reynolds stress, a measure of the amount of energy initially in the shear flow of the equilibrium model which is transferred to the disturbance. It is given by

$$\sigma_R = -\rho_\circ \varpi (\frac{\partial \Omega}{\partial \varpi}) \langle \delta v_\varpi \delta v_\phi \rangle \,. \tag{32}$$

The stress σ_Π measures the redistribution of energy within the toroid by acoustic wave fluxes carried by the disturbance. It is given by

$$\sigma_\Pi = -\nabla \cdot \langle \delta \mathrm{P} \delta \mathbf{v} \rangle \,. \tag{33}$$

σ_Φ is a measure of the work performed on the disturbance by gravitational forces. It is given by

$$\sigma_\Phi = -\rho_\circ \langle \delta \mathbf{v} \cdot \nabla(\delta\Phi_d) \rangle \,. \tag{34}$$

The terms in the energy equation indicate where instability is driven and where it is damped. For normal modes, the growth time in terms of work integrals is given by

$$\tau = 2\frac{\int \langle \mathcal{E} \rangle \, d^3x}{\int (\sigma_R + \sigma_\Phi) d^3x}. \tag{35}$$

The acoustic wave flux term σ_Π does not appear in the expression for τ because it goes to zero at the surface and so integrates to zero over the volume of the toroid.

4. STABILITY RESULTS

4.1. Linear Regime

4.1.1. Eigenvalues and Eigenfunctions

We map the stability regions for toroids in $T/|W|$-space in this section. To facilitate comparison with previous workers, oscillation frequencies and growth rates for given m, ω_m and τ_m^{-1}, are also given in the dimensionless forms

$$y_1(m) = \frac{|\omega_m|}{\Omega_{max}} - m, \text{ and } y_2(m) = \frac{1}{\tau_m \Omega_{max}} \tag{36}$$

(Kojima 1986). If $y_1(m) < 0$, corotation falls outside the density maximum and if $y_1(m) > 0$, corotation falls inside the density maximum. The eigenvalues for the m = 1, 2, 3, and 4 modes for $n = 3/2$ toroid sequences with q = 1, 3/2, and 2 are presented in Figure 1. We discuss the (n, q) = (3/2,3/2) toroid sequence as representative of general toroid behavior. Instability first sets in at $T/|W| \approx 0.163$ through $m = 2$ barlike modes. The barlike modes dominate until $T/|W| \sim 0.25$ is reached. The growth rate of the barlike modes, $y_2(2)$, initially increases strongly after threshold is passed. The rate of increase slows beyond $T/|W| \sim 0.18$, peaks near $T/|W| \approx$ 0.22-0.23, and then declines until it approaches 0 around $T/|W| \approx$ 0.25-0.26. Over this range the normalized oscillation frequency of the barlike modes is nearly constant, $y_1(2) \sim$ -1.1 near threshold, increasing only slowly to -0.91 at $T/|W| \sim 0.25$. Corotation for these barlike I modes falls well outside the location of ρ_{max}, $R_{co} \sim$ 1.5-1.6 R_{max}.

Over this region, one-armed spirals ($m = 1$ modes) are also unstable. For $T/|W| < 0.22$, there are two types of $m = 1$ modes, one with fast oscillation frequency $y_1(1) \sim +1$ and one with slow oscillation frequency $y_1(1) \sim$ -1. Corotation falls near the inner edge of the toroid for the fast mode and beyond the outer edge of the toroid for the slow mode. These modes may be the inner and outer edge I modes discussed in Christodoulou (1994). The slow $m = 1$ mode dominates the fast $m = 1$ mode for $T/|W| \lesssim 0.22$. However, for $T/|W| < 0.22$, the $m = 1$ growth times are long. For example, the slow and fast modes for the $T/|W| = 0.192$ toroid have e-folding times of $\tau_1 \sim 5$ and 10 τ_{max}, respectively. For $T/|W| \gtrsim 0.225$, the growth rates for $m = 1$ modes are fast, $\tau_1 \lesssim 1.5\ \tau_{max}$. In fact, for $T/|W| \gtrsim 0.25$, $m = 1$ modes overtake and dominate the barlike I

mode. However, around where the $m = 1$ modes start to dominate the barlike I modes, another set of low-m nonaxisymmetric modes appears, the J modes with instability thresholds of $T/|W|$ $\sim$ 0.25-0.26, 0.23-0.25, and 0.25-0.26 for $m = 2$, 3, and 4, respectively. In the transition region which separates the I and J instability regimes, $m = 1$ modes, as just noted, dominate. Although weak, $m = 2$ modes are also unstable in the transition region showing multiple oscillation modes for given m. Outside the I/J mode transition region, unstable modes show simple behavior with evolutions dominated by single modes for given m.

The $m = 3$ J mode dominates the $m = 1$ mode for $T/|W| \gtrsim 0.26$. It, in turn, gives way to the $m = 4$ J mode for $T/|W| \gtrsim 0.28$. Beyond threshold, all J modes have faster normalized pattern frequencies than do the lower I modes. For the barlike J modes, the ω_2 are roughly twice those found for the barlike I modes. The barlike J modes have $y_1(m) \sim$ -0.2 to 0.2 with corotation radii close to their density maxima, $R_{co}/R_{max} \approx$ 0.95-1.1. The stability limits in $T/|W|$-space and the location of corotation are consistent with the suggestion that the lower $T/|W|$ modes are I modes and that the higher $T/|W|$ modes are J modes, although there is uncertainty about this identification for the $m = 2$ modes in $T/|W| < 0.19$ toroids (see below).

Near the transition region separating the I and J modes, $m = 1$ modes, as noted above, dominate the barlike modes. Although weak, $m = 2$ modes are also unstable in the transition region showing multiple unstable modes for given m, all of which show slow growth rate, $\tau_2 \gtrsim ... \tau_{max}$. Outside the I/J mode transition region, $m = 2$ modes show simple behavior with evolutions dominated by single modes, the I and J modes discussed above.

The locations of the instability thresholds for I and J modes in $T/|W|$-space are not qualitatively affected by q, the exponent of the angular velocity distribution. The quantitative locations of the instability thresholds in $T/|W|$-space and the widths of the I to J mode transition regions, however, depend on q. Instability sets in through barlike modes for all q, setting in first for $q = 3/2$ toroids, then for $q = 2$ toroids, and lastly for $q = 1$ toroids (see Figure 1). For both I and J modes, the difference in $T/|W|$ for the instability thresholds as a function of q is small; the thresholds are the same to within 0.02 for $q = 1$, 3/2, and 2. The onset of instability in toroids before $T/|W| = 0.274$ is reached, the commonly quoted stability limit for barlike modes in polytropes, was predicted by Hachisu, Tohline, & Eriguchi (1987), and verified by Tohline & Hachisu (1990). Hachisu, Tohline, & Eriguchi argued that gravitationally driven instabilities set in when the ratio of the local free-fall time, $\tau = \sqrt{3\pi/32G\rho}$ and the sound crossing time $\tau_s = 2\pi\varpi/c_s$, where c_s is the local sound speed, fell below 0.08-0.11. Based on this argument, they predicted that toroids would be unstable for $T/|W| \gtrsim 0.184$, 0.151, and 0.142 for $q = 1$, 3/2, and 2. Hachisu, Tohline, & Eriguchi argued that the effects of the Coriolis force were responsible for the shift of the stability limits to higher $T/|W|$ for the smaller q; Coriolis forces weaken with increasing q. The Hachisu, Tohline, & Eriguchi prediction for $q = 1$ is close to that which we found; $q = 1$ toroids are unstable for $T/|W| \gtrsim 0.18$. The other predictions are less accurate. We find limits of $T/|W| \sim 0.163$ and 0.17 for $q = 3/2$ and 2 toroids.

How the geometric properties of the eigenfunctions change with increasing $T/|W|$ is discussed next with particular attention paid to the differences in appearance of I and J modes. We again look at $(n, q) = (3/2,3/2)$ toroids as representative of toroid behavior. The relative density eigenfunctions $|\delta\rho/\rho_\circ|$ and its constant phase locus in the equatorial plane for representative (3/2,3/2) toroids are presented in Figure 2. In addition, we also show the eigenfunction

$$\mathcal{W} = \delta h + \delta\Phi_g = \gamma \left(\frac{P_\circ}{\rho_\circ^2}\right) \delta\rho + \delta\Phi_g \tag{37}$$

and its constant phase locus in Figure 2. Here, δh is the perturbed enthalpy. Both $|\delta\rho|/\rho_\circ$ and $\mathcal{W}$ are normalized to their peak values for presentation in the figures. $\mathcal{W}$ is a useful representation particularly near the instability threshold as can be seen from the dispersion relation for eigenmodes with time and azimuthal dependence given by $\mathrm{e}^{i(m\phi-\omega t)}$,

$$\sigma\delta\rho = (\frac{1}{\varpi})\frac{\partial}{\partial\varpi}\left[\frac{\varpi\rho_\circ}{D}(\sigma\frac{\partial}{\partial\varpi} - \frac{2m\Omega}{\varpi})\mathcal{W}\right] + \frac{\partial}{\partial z}\left[\frac{\rho_\circ}{\sigma}\frac{\partial}{\partial z}\mathcal{W}\right] + \left[\frac{m\rho_\circ\kappa^2}{2\varpi\Omega D}\frac{\partial}{\partial\varpi} - \frac{m^2\rho_\circ\sigma}{\varpi^2 D}\right]\mathcal{W}. \tag{38}$$

Here, $\sigma = \omega - m\Omega$, $D = \kappa^2 - \sigma^2$, and κ, the epicyclic frequency, is given by

$$\kappa^2 = 2(2-q)\Omega^2 \tag{39}$$

for power law $\Omega(\varpi)$. Corotation falls where the real part of σ, σ_R is equal to zero. The inner and outer Lindblad resonances fall where $\sigma_R \pm \kappa = 0$. For power law $\Omega(\varpi)$, the Lindblad resonances and the location of corotation are related as

$$\frac{R_{LR}}{R_{co}} = \left(\frac{m}{m \pm \sqrt{4-2q}}\right)^{-1/q}. \tag{40}$$

For toroids with constant specific angular momentum ($q = 2$), $\kappa^2 = 0$, $D = \sigma^2$, and corotation and the Lindblad resonances are degenerate. We show these and the critical radii mentioned in §2 for the $m = 2$ barlike modes for $q = 1$, 3/2, and 2 toroid sequences in Figure 3. In Figures 4 and 5, we show the time-averaged energies and stresses, the time-averaged angular momenta, and the time-averaged self-interaction torques γ for the modes shown in Figure 2.

First, consider the $m = 2$ barlike modes over the I mode range $0.16 \lesssim T/|W| \lesssim 0.26$. For the $T/|W| = 0.163$ toroid, the relative density eigenfunction $|\delta\rho/\rho_\circ|$ shows a phase shift of $\delta \sim \pi/3$ inside R_{co}. The radius where $|\delta\rho/\rho_\circ|$ exhibits its sharp minimum is labeled R_ϕ. The perturbed toroid is well-described as a coherent central bar which undergoes a sharp phase advance at R_ϕ, outside of which its figure settles into another coherent bar which extends to its outer edge. The phase swing at R_ϕ falls inside R_{max}, R_γ, R_λ, and both Lindblad resonances as well as inside R_{co}. The inner Lindblad resonance R_{ILR} does fall near R_{max}. Suggestively, the phase change at R_ϕ is roughly where the Toomre Q-parameter first drops below unity as one moves outward from the inner edge of the toroid. The eigenfunction $\mathcal{W}$ also shows a sharp minimum whose location we designate $R_\mathcal{W}$. $\mathcal{W}$ varies smoothly through R_ϕ with a shallow, smooth minimum near R_{co}, between R_ϕ and R_+. With increasing $T/|W|$, $R_\mathcal{W}$ remains close to R_{co} but moves away from R_γ.

The minimum in $\mathcal{W}$ smooths beyond threshold because resonances are weakened when instability becomes stronger. By $T/|W| = 0.19$, $\tau_2/P_2 \sim 0.25$. This is in contrast to the minimum in $|\delta\rho/\rho_\circ|$ which remains sharp beyond threshold; the $|\delta\rho|$ minimum is apparently not related to a resonance.

Although we identify the low $T/|W|$ barlike modes as I modes, we note that the $m = 2$ eigenmodes change character at $T/|W| = 0.19$. Interestingly, the toroid with $T/|W| = 0.19$ is the one for which the outer Lindblad resonance first moves outside the disk. The spiral arms of the eigenfunctions switch from leading to trailing for toroids with $T/|W| > 0.19$ with perturbed figures nicely modeled as coherent central bars with rapid $\pi/2$ phase lags at R_ϕ followed by nearly coherent bars to the outer edges of the toroids. With increasing $T/|W|$, R_ϕ continues to fall inside R_γ, R_{co}, and R_λ while R_{ILR} continues to fall near R_{max}. Corotation, again, does not coincide with any of these critical radii except for perhaps $R_\mathcal{W}$. In particular, the location of the vortensity extremum, R_λ does not lie on or track either R_{co} or R_{ILR}. The $m = 2$ modes are not related to the resonant modes of self-gravitating thin disks discussed by Papaloizou & Savonije (1991), such as vortensity modes where R_λ sits right on R_{co} at threshold in order to neutralize the corotation singularity, and corotation modes, modes where the region where $Q < 1$ tightly brackets corotation.

Representative $m = 1$ eigenfunctions over this range are shown in Figure 6. $\mathcal{W}$ and $|\delta\rho|/\rho_\circ$ eigenfunctions are similar in form to the $m = 2$ modes of $T/|W| > 0.19$ toroids. The $|\delta\rho|/\rho_\circ$ show sharp minima slightly outside the location of ρ_{max}, $R_\phi = 1.17\ R_{max}$ at which the eigenmode exhibits a rapid phase change of order π. $\mathcal{W}$ for the $T/|W| = 0.192$ toroid shows a sharp minimum at $0.66\ R_{max}$, just outside corotation $R_{co} = 0.63\ R_{max}$. For the $T/|W| = 0.253$ toroid, $\mathcal{W}$ shows a shallower minimum at $R_\mathcal{W} = 0.68\ R_{max}$. $R_\mathcal{W}$ again falls near corotation. Based on the appearance of the mode and location of these and other key radii, it appears that the $m = 1$ modes are related to I modes (see Christodoulou 1994) rather than to the *eccentric* $m = 1$ modes of Adams, Ruden, & Shu (1989). This is expected because the *eccentric* mode of Adams, Ruden, & Shu relies on a central star moving in response to the growth of eccentricity in the disk (although see Noh, Vishniac, & Cochran 1992, Taga & Iye 1994).

Barlike $m = 2$ J modes emerge around $T/|W| \sim 0.26$. At threshold, the $m = 2$ J mode eigenfunctions show distinct differences in appearance from the I modes. At threshold, the phase lag sharpens and the $|\delta\rho|/\rho_\circ$ eigenfunction resembles the one for the $T/|W| = 0.19$ toroid. It shows a coherent barlike structure inside R_{max}, the location of the $\pi/2$ phase lag. Outside of R_{max} the eigenfunction settles into another coherent barlike structure which persists to the outer edge of the toroid. $\mathcal{W}$ shows a similar structure except that it exhibits a rapid $\pi/2$ phase lag at R_{co}. Beyond threshold, the eigenfunctions continue to show $\pi/2$ phase lags but the transitions are smoother, more rounded than for the $m = 2$ I modes of the lower $T/|W|$ toroids and for the toroid near threshold. Perturbed toroids continue to show coherent central bars, but the outer bars now trail smoothly into pairs of loosely wound spiral arms. Because the dimensionless oscillation frequencies of J modes are much faster than for the $m = 2$ I modes, corotation falls close to R_{max}. The location of the phase swing, R_ϕ, also coincides with R_γ, R_{co}, $R_\mathcal{W}$, and R_λ

for these high $T/|W|$ modes and Lindblad resonances re-appear. The Lindblad resonances are roughly symmetrically placed about R_{co} for the $T/|W| = 0.273$ toroid. As $T/|W|$ increases, the Lindblad resonances move away from R_{co} and both fall outside the toroid for $T/|W| > 0.30$. Q-barriers, the locations where Q passes through 1, now tightly bracket corotation increasing the possibility of wave *tunneling* through corotation and amplification through the *super*-reflection of waves. Further, examination of the time-averaged angular momentum for the $m = 2$ modes of these toroids shows that the angular momentum carried by the eigenmodes changes sign at R_ϕ (see Figure 4). This behavior is not seen in the I modes. The change in sign of the angular momentum is consistent with the suggestion that instability is driven by the coupling of waves across the corotation singularity (*e.g.,* see Nakagawa & Sekiya 1994).

Goodman & Narayan (1988) performed an analytical analysis of self-gravitating, two-dimensional, incompressible slender annuli with angular momentum profiles similar to those used here in which they showed that a strict demarcation line between I and J modes could be made based on R_{co}. I modes were shown to have $R_{co} > R_+$, that is, R_{co} fell outside the disk, while J modes were shown to have $R_{co} = R_{max}$. Our models show similar behavior in that: (i) there is a transition in the location of corotation and growth rates for hot, self-gravitating toroids, however, the change is gradual. (ii) Our models show that corotation falls outside R_{max} for I modes and near R_{max} for J modes. However, only the I mode for the model just below the critical $T/|W|$ shows $R_{co} > R_+$. For toroids beyond the critical $T/|W|$, R_{co} quickly approaches R_{max}. For higher $T/|W|$ models, R_{co} asymptotically approaches R_{max} as $T/|W|$ increases. For $q = 3/2$ and 2 toroids, it is clear roughly where the transition from I modes to J modes occurs, based on the eigenvalues. However, recall that away from threshold and the transition region, a clean distinction between I and J modes based on the appearance of their eigenfunctions cannot be made.

4.1.2. $\langle \mathcal{E} \rangle$ and the Work Integrals

The perturbed kinetic energy $\mathcal{E}_k$, the perturbed enthalpy $\mathcal{E}_h$, and the stresses σ_R, σ_Φ, and σ_Π for the $m = 2$ modes shown in Figure 2 are presented in Figure 3. For toroids with $T/|W| < 0.19$, the kinetic energy growth rate $2(\mathcal{E}_k/\tau)$ and the acoustic wave stress σ_Π peak at the same radius while the enthalpy growth rate $2(\mathcal{E}_h/\tau)$ and the Reynolds stress σ_R peak at the same radius. The $2(\mathcal{E}_k/\tau)$ peak falls closer to the inner edge of the toroid than does that of $2(\mathcal{E}_h/\tau)$. The enthalpy growth rate $2(\mathcal{E}_h/\tau)$ shows a second smaller peak outside R_{max} which grows in size and importance as $T/|W|$ increases. For these low $T/|W|$ toroids, the strongest driving occurs near the inner edge of the toroid. Notice that the gravitational stress σ_Φ peaks near R_{max} and that σ_Π is negative where σ_Φ is the largest. The region where $\sigma_\Pi > 0$ where energy is transferred from the background flow to the perturbation, is also where $Q > 1$. For toroids with $T/|W| > 0.19$, the secondary peak in $2(\mathcal{E}_k/\tau)$ increases in size relative to the main inner peak, and σ_R and σ_Φ increase in importance compared to σ_Π. σ_Π is now positive near the inner and outer edges of the toroid and < 0 where σ_Φ peaks. σ_R continues to peak close to the inner edge of the toroid.

It is also now more obvious that σ_Φ peaks where $(\mathcal{E}_k + \mathcal{E}_h)$ reaches a local maximum, which falls near ρ_{max}. The large region where $\sigma_\Pi < 0$ is the region where $Q < 1$.

For the $T/|W| > 0.25$-0.26 toroids, where J modes dominate, the enthalpy term $2(\mathcal{E}_h/\tau)$ shows two strong maxima. Near threshold, the maximum near the inner edge of the toroid dominates but as $T/|W|$ increases the two maxima become more comparable in size. This is consistent with the fact that the $Q < 1$ region narrows around density maximum for $T/|W| > 0.25$-0.26. σ_Φ, the gravitational stress, peaks at the minimum in $2(\mathcal{E}_h/\tau)$, where σ_Π is the most negative. This is also near the density maximum which suggests that gravity puts energy into the disturbance at the maximum density and drives instability. The Reynolds stress still peaks where $2(\mathcal{E}_K/\tau)$ peaks, but its amplitude is much smaller in comparison to σ_Φ than for the low $T/|W|$ toroids.

We show $\mathcal{R} = \int \sigma_\Phi \mathrm{d}^3x / \int \sigma_R \mathrm{d}^3x$ in Figure 7. $\mathcal{R} \sim 2$ for toroids with $T/|W| < 0.25$-0.26 toroids. For toroids with larger $T/|W|$, $\mathcal{R}$ is larger, $\mathcal{R} > 4$ for toroids with $T/|W| > 0.26$. This behavior is consistent with the suggestion that the high $T/|W|$ modes are the gravity driven J modes, and the low $T/|W|$ modes are the I modes, modes *intermediate* in nature between the shear-driven P modes and the gravity driven J modes.

4.2. Nonlinear Regime

Simulations of $(n, q) = (3/2{,}3/2)$ toroids with $T/|W| = 0.192$, 0.253, and 0.272 were run to investigate whether I and J modes lead to prompt fission. The set of toroids was chosen because the first was dominated by the barlike I mode, the second by a one-armed spiral mode, and the third by $m \geq 3$ J modes. Each simulation is described in the following sections but note that in no case did prompt fission occur as a result of nonaxisymmetric instability. Our $T/|W| = 0.192$ results are consistent with those presented in Tohline & Hachisu (1990) and Woodward, Tohline, & Hachisu (1994) who also found that even-m I modes did not lead to prompt fission in the toroids they tested.

4.2.1. $T/|W| = 0.192$ Toroid

$T/|W| = 0.192$ toroids are unstable to the $m = 2$ barlike mode and weakly unstable to the $m = 1$ mode in the linear regime. These results carry over to nonlinear perturbations as can be seen in Figure 9 where we show the evolution of the amplitudes of low m nonaxisymmetric disturbances, $\mathcal{A}_m$, for the nonlinear simulation. In addition, we include $T/|W|$ and $\cos(\phi_\rho)$ for the $m = 2$ barlike mode at three radii in the equatorial plane in the Figure. The amplitudes, $\mathcal{A}_m$, are related to the Fourier powers of each m-mode (see Pickett, Durisen, & Davis 1996 for a description of the $\mathcal{A}_m$), and ϕ_ρ is the phase for the $m = 2$ density disturbance. All low-m nonaxisymmetric disturbances participate in an early *settling* phase during which their amplitudes grow to sizes $\sim 10^{-5}$ where they level off. During this settling phase, the toroid initially expands, both inwardly

and outwardly, but quickly re-settles into an equilibrium nearly identical to that of the original model. This transient phase is likely driven by a slight adjustment of the equilibrium model caused by the development of meridional motions. The original equilibrium model is assumed to rotate on cylinders with no meridional velocity components. In the nonlinear simulation meridional motions arise right after the simulation is started. The kinetic energy in the meridional motions is small, but not zero; it is < 0.01 % of the energy contained in rotational and thermal motions.

An $m = 2$ barlike mode organizes soon after the initial settling phase and starts to grow exponentially around $t \sim 0.5\tau_{max}$. It settles into fully global growth by $t =$ 2-3 τ_{max}. Eigenvalues for the barlike mode are nearly identical to those we find for the linear barlike mode. We find pattern period $P_2 = 2.0\ \tau_{max}$ and growth time $\tau_2 \sim 0.57\ \tau_{max}$, in excellent agreement with the linear eigenvalues, $P_2 = 2.09\ \tau_{max}$ and $\tau_2 = 0.515\ \tau_{max}$. [1] The relative density eigenfunction $|\delta\rho/\rho_\circ|$ strongly resembles the linear eigenfunction at this time (compare Figures 2 and 10). $|\delta\rho/\rho_\circ|$ shows maxima at the inner and outer edges of the toroid with a sharp minimum at $R_\phi = 0.7\ R_{max}$, which marks the location of the $\pi/2$ phase shift in the figure of the bar. Corotation falls at $R_{co} = 1.6\ R_{max}$.

During the early portion of the simulation as the barlike mode organizes, mass and angular momentum flow neither inward nor outward consistently. They flow alternately inward and outward across $R \sim 1.3\ R_{max}$, close to the radius where the quasi-linear (QL) γ changes sign, $R_\gamma = 1.37\ R_{max}$. Eventually as the barlike mode settles and grows in amplitude, the mass and angular momentum flows settle into steady patterns in which they transport mass and angular momentum across $0.87\ R_{max}$, near the radius where the rapid phase swing in $\delta\rho$ occurs and where the angular momentum of the linear eigenfunction changes sign. The mass (loss/gain) rate, $(\Delta m_c/\Delta t)$, and the torque, the net flow of angular momentum into and out of a given volume γ, at $t = 4.54\ \tau_{max}$ when $\mathcal{A}_2 = 0.23$, are shown in Figure 11. The nonlinear self-interaction gravitational torque, γ_{nl}, has a form similar to that of the QL γ (see Equation [28] and Figure 4). When the bar amplitude is growing, the outer region of the toroid gains angular momentum at the expense of the central region which loses angular momentum, in general. The sign change occurs near $1.37\ R_{max}$. However, significantly, $\gamma > 0$ in a small region near the inner edge of the toroid where the angular momentum perturbation of the barlike mode is < 0. The self-interaction torque slows the inward spread of the toroid and the structure remains similar to that of a toroid as instability develops into the nonlinear regime.

Nonlinear effects markedly start to alter the structure of the toroid after the bar surpasses amplitude $\mathcal{A}_2 \sim 0.1$ which occurs around $t = 4.1\ \tau_{max}$. At $t = 4.1\ \tau_{max}$, the amplitudes of even $m > 2$ disturbances start to grow. These even m disturbances have the same pattern period as does the $m = 2$ mode and are likely the result of a nonsinusoidal $m = 2$ waveform. The $m = 2$ disturbance eventually saturates when its amplitude reaches $\mathcal{A}_2 \sim 0.96$ at $t \sim 5.6\ \tau_{max}$.

[1] The $m = 1$ mode is marginally unstable in the linear regime. There are two $m = 1$ modes one with short pattern period $= 0.49\ \tau_{max}$ and one with long pattern period $\sim 5\ \tau_{max}$. Both have long growth times, $\tau_1 \gtrsim 5\ \tau_{max}$.

Imamura *et al.* (2001) showed that saturation of barlike f modes in polytropes was caused by the gravitational self-interaction torque γ described in §3.2 (Equation [28]). Self-interaction torques led to the ejection of significant mass from the polytrope which formed a circumstellar disk; the remaining mass then lost angular momentum to the disk until the central object reached a configuration marginally stable to the barlike instability. Given this and the QL torque given by Equation (28), Imamura *et al.* suggested that the barlike mode would grow until the angular momentum transport time

$$\tau_j = \left| \frac{j_b - j_{lim}}{\gamma} \right|, \tag{41}$$

where j_b is the angular momentum contained in the region inside R_γ and j_{lim} is the angular momentum of the marginally stable axisymmetric object with M_b was comparable to the mode's growth time; a result confirmed by their nonlinear simulations. If this supposition also holds for toroids, then we would expect that the mass inside R_γ would shed j until it reached the j of a toroid (or other oblate figure) marginally stable to the barlike instability. We test this suggestion using the QL γ and the peak $\mathcal{A}_2$ from the nonlinear simulation, estimates for the bar mass M_b (=0.629) and angular momentum j_b (=0.395) based on our quasi-linear theory, and the angular momentum for the marginally stable toroid J_{lim} (=0.332), based on our linear analysis. Given these numbers, and if we assume that the shortest plausible transport time scale is given by how long it takes the bar to lose enough j to approach the marginally stable axisymmetric state and that the longest possible transport time scale is the time it takes the toroid to transfer its entire j, then τ_j should obey $0.40\ \tau_{max} < \tau_j < 2.7\ \tau_{max}$. We find that the barlike mode has growth time $\tau_2 \sim 0.57\ \tau_{max}$ in our nonlinear simulation, consistent with the suggestion that the barlike instability tries to drive the toroid to its marginally stable axisymmetric configuration. Doubt may be cast on our conclusion, however, because by the time saturation is reached, the toroid has spread significantly and our QL model is becoming less accurate. Our conclusion is buttressed, however, by our nonlinear results. We find that as the barlike mode approaches saturation, γ_{nl} still resembles the QL γ, with only quantitative differences appearing. Recall that the torque γ_{nl} at $t = 4.54\ \tau_{max}$ when $\mathcal{A}_2 = 0.23$ (Figure 11) has a form similar to that of the QL gravitational self-interaction torque γ shown in Figure 4. If we use γ_{nl} to estimate the angular momentum transport time scale, we find τ_j obeys $0.2\ \tau_{max} < \tau_j < 1.2\ \tau_{max}$, similar to the prediction based on our QL theory. Just as for the filled-center polytropes studied by Imamura *et al.* (2000), the gravitational self-interaction torque appears to be a viable saturation mechanism for barlike modes in toroids.

After saturation, γ_{nl} changes character as $\mathcal{A}_2$ starts to fall. R_Υ remains at $1.37\ R_{max}$ but the region inside R_γ now gains angular momentum and the region outside R_γ loses angular momentum. Following saturation, $\mathcal{A}_2$ falls and the bar reaches a minimum at $\mathcal{A}_2 \sim 0.47$ around $t \sim 6.9\ \tau_{max}$, after which it rebounds and γ_{nl} reverts to its original form where the region inside $R_\gamma \sim 1.37\ R_{max}$ loses angular momentum and the region outside R_γ gains angular momentum. The barlike mode reaches its second maximum, $\mathcal{A}_2 \sim 0.95$, around $t \sim 7.5\ \tau_{max}$ where γ_{nl} again pivots about $1.37\ R_{max}$ and another small disk is ejected. The toroid continues to follow this

slow damping, oscillatory pattern until $t \sim 9\ \tau_{max}$ when the damping rate increases, $T/|W|$ starts to increase, and the evolution of the central region changes from one which resembles a damping toroidal instability to one characterized as a secular change to a new equilibrium state, a filled-center polytrope equilibrium. The central region starts to rotate in the retrograde sense with a strong increase in the outward mass flux and an outward pulse of negative angular momentum. The mass and angular momentum redistribution permanently alter the structure and specific angular momentum distribution of the central object. Around $t \sim 12\ \tau_{max}$, $T/|W|$ stops growing and the simulation settles to a configuration approaching a distorted, stable, steady star/disk system. We stop the simulation at $t \sim 19\ \tau_{max}$.

The final state has $\mathcal{A}_2 \sim 0.12$ and $T/|W| \sim 0.193$, well beyond the instability threshold for $(n, q) = (3/2,3/2)$ toroids but below the threshold of $T/|W| = 0.27$ for barlike instabilities in star-like polytropes. The central object has a core in near uniform rotation with an envelope with power law angular velocity distribution, $\Omega \propto \varpi^{-1.1}$. The central object has an off-center density maximum. The uniformly rotating core contains $\sim$ 10-12 % of the mass with the transition to the uniform velocity region falling near $\varpi \sim 0.5\ R_{max}$. The central object is surrounded by a low mass disk. The transition region between the central object and the disk where the angular velocity increases contains 0.75 % of the mass and $\sim$ 1.6 % of the angular momentum. The disk contains 0.65 % of the mass and $\sim$ 2.7 % of the angular momentum with $\Omega \propto \varpi^{-1.75}$. The barlike instability did not lead to a prompt disruption of the toroid.

4.2.2. $T/|W| = 0.253$ Toroid

The $(n, q) = (3/2,3/2)$ toroid with $T/|W| = 0.253$ sits in $T/|W|$-space where fast $m = 1$ modes are expected to dominate; the region where the $m = 2$ I mode has nearly disappeared, but before where strong $m > 2$ J modes appear. In our linear analysis, we find eigenvalues $(P_m/\tau_{max}, \tau_m/\tau_{max}) = (0.52,0.40)$, (1.80,1.16), and (1.19,0.71) for the $m = 1$, 2, and 3 modes, respectively. Our expectations are borne out by the nonlinear simulation. We show time histories for the low-m $\mathcal{A}_m$, $T/|W|$, and cos ϕ_ρ from our nonlinear simulation in Figure 12. As for the $T/|W| = 0.192$ simulation, the $\mathcal{A}_m$ grwo quickly to amplitudes of $\sim 10^{-5}$ where they level off. During the transient, the toroid structure adjusts slightly but quickly settles into an equilibrium state nearly identical to that of the original model. The $m = 1$ mode is the first to organize falling into steady exponential growth by $t \sim 1\ \tau_{max}$ with $(P_1/\tau_{max}, \tau_1/\tau_{max}) = (0.53,0.38)$ in excellent agreement with the linear analysis. Also, as in the linear analysis, a slow barlike mode develops at early times giving way to a faster barlike mode at later times. The slow oscillation mode has $P_2 \sim 2\ \tau_{max}$ which maintains itself for around two cycles before giving way to the faster oscillation mode with pattern period $\sim$ 0.3-0.4 τ_{max} at $t \sim 3.2\ \tau_{max}$. Also, around 3.2 τ_{max}, an $m = 3$ disturbance develops. The $m = 2$ and 3 disturbances have growth times of $(\tau_m/\tau_{max}) = 0.45$ and 0.58, respectively. Although $m > 2$ modes grow, they are dominated by the $m = 1$ mode. The $m = 3$ growth time is roughly consistent with the linear result, but the growth in $m = 2$ is faster.

Both the $m = 1$ and 2 mode eigenfunctions found in the nonlinear simulation at early time are nearly identical in form to those found in the linear simulation. To show this, we present the $m =$ 1, 2, and 3 linear eigenmodes in Figure 13 and the $m = 1$ and 2 $|\delta\rho/\rho_\circ|$ eigenfunctions and their constant phase loci in the equatorial plane for $t \sim 3\ \tau_{max}$ in Figure 14.

Strong nonlinear effects appear around $t = 3.2$-$3.3\ \tau_{max}$, when the $m = 1$ mode amplitude $\mathcal{A}_1$ reaches 0.1. At this time, $T/|W|$ starts to fall (see Figure 13) and the toroid starts to separate into two rings (see Figure 15 where we show the evolution of the cylindrical mass m_c distribution). As for the $T/|W| = 0.192$ toroid, the early nonlinear evolution is dominated by the gravitational self-interaction torque arises which efficiently redistributes angular momentum in the evolving toroid. The form for γ strongly resembles that predicted by the QL theory. γ_{nl} is negative in the inner region of the toroid and positive in the outer region of the toroid. This similarity continues to hold qualitatively even after the toroid becomes strongly nonlinear. In fact, the form for the torque remains consistent with the QL theory even after the center of the toroid has filled-in and an ejected low mass disk whose outer edge lies a nearly three times the original radius of the toroid has formed.

Gravitational self-interaction torques appear to play strong roles in the growth of nonaxisymmetric instabilities in the early nonlinear regime. However, because the quantitative comparison comparison between the QL γ and γ_{nl} is not good, the link cannot be made as convincingly as for the $T/|W| = 0.192$ toroid. Nonlinear effects exerted on the $T/|W| = 0.253$ toroid develop much more quickly in the $T/|W| = 0.253$ toroid compared to the $T/|W| = 0.192$ toroid. The different (stronger) effects of the self-gravitational torque on the $T/|W| = 0.253$ toroid than on the $T/|W| = 0.192$ toroid can be understood from examination of the perturbed angular momentum δJ of the $m = 1$ mode (see Figure 7) and the QL γ. The δJ is divided into two regions each carrying opposite signed δJ. The region where $\delta J < 0$ matches the region where $\gamma < 0$. Consequently, as the $m = 1$ mode becomes nonlinear, the self-interaction torque tends to enhance growth near the inner edge of the toroid leading to the rapid development of nonlinear effects. This differs from the $T/|W| = 0.192$ toroid where δJ has a strong negative peak near the inner edge of the toroid, is small in the central region of the toroid with a shallow, broader peak in the outer part of the toroid and γ shows a a small positive region which coincides with where $\delta J < 0$. The early nonlinear growth of the $m = 2$ mode in the $T/|W| = 0.192$ toroid is slowed by the action of the self-interaction torque.

The $m = 1$ mode saturates at $\mathcal{A}_1 = 0.54$ when $t = 4.8\ \tau_{max}$ and $T/|W|$ has fallen to 0.20. By this time the central edge of the toroid has collapsed and the center of the toroid has filled in. After saturation, the $m = 1$ mode oscillation period changes increasing to $\sim 0.78\ \tau_{max}$. After saturation, as the $m = 1$ mode weakens, the barlike disturbance continues to grow, surpassing $\mathcal{A}_1$ around $t \sim 4.9\ \tau_{max}$. The barlike mode peaks at time $t = 5.2\ \tau_{max}$ when $\mathcal{A}_2 = 0.81$. During this time, the $m = 1$ mode rebounds. The $m = 1$ mode becomes larger the barlike mode at $t =$ $5.6\ \tau_{max}$. We follow the evolution until $t \sim 5.7\ \tau_{max}$ when $\mathcal{A}_1 \sim 0.3$-0.4. At this time, $m = 1$ shows no indication that it is damping. The further long-term behavior is uncertain however. The

simulation was stopped because after the center of the toroid had filled-in, energy conservation was poor, the toroid had lost 15 % of its energy by this time.

4.2.3. $T/|W| = 0.272$ Toroid

The $(n, q) = (3/2,3/2)$, $T/|W| = 0.272$ toroid is representative of models dominated by $m > 2$ J modes, rather than I modes. Several low-order modes are unstable in the linear regime. Pattern periods and growth times for the low m-modes in the linear regime are $(P_m/\tau_{max}, \tau_m/\tau_{max}) =$ (0.507,0.293), (1.14,0.547), (1.11,0.205), and (1.10,0.248) for $m = 1$, 2, 3, and 4, respectively. We show the linear low-m mode density eigenfunctions in Figure 16. The $m = 3$ mode has the fastest growth rate and is expected to dominate in the nonlinear regime. Our nonlinear simulation bears out this expectation. See Figure 17 where we show the $\mathcal{A}_m$, $T/|W|$, and the $m = 1$ to 4 cos ϕ_m time histories for our nonlinear simulation. Initially, there again is a *settling* period during which the power in all low m modes grows as the toroid adjusts to a slightly altered equilibrium state. Growth in $m = 1$, 3, and 4 starts after $t \sim 0.7\ \tau_{max}$. Growth in $m = 2$ is not detected. The $m = 3$ mode organizes most quickly and dominates the simulation. The $m = 1$ and 4 modes organize and grow more slowly than does the $m = 3$ mode. The disturbances settle into steady growth by $t \sim 1$ τ_{max}. For early times, we find $(P_m/\tau_{max}, \tau_m/\tau_{max}) = (0.49,0.28)$, (1.14,0.21) and (1.15,0.26) for $m = 1$, 3, and 4, respectively. The eigenvalues are in excellent agreement with the linear results, all are within 4 % of the linear eigenvalues. The $m = 3$ eigenfunction in the equatorial plane for time $t = 1\ \tau_{max}$, when $\mathcal{A}_3 \sim 0.1$, is shown in Figure 18. The nonlinear eigenfunction strongly resembles the linear one (see Figure 16) with maxima at the inner and outer edges of the toroid and a rounded minimum near density maximum, $\varpi \sim 0.65\ R_{max}$. Corotation for $m = 3$ falls at nearly the density maximum, $R_{co} \sim 1.1\ R_{max}$, characteristic of a J mode. The angular momentum redistribution function γ_{nl}, quickly settles into a steady form. γ_{nl} is qualitatively similar in form to the linear γ where angular momentum is generally transferred from the inner region to the outer region. There is a slight difference however in that the inner edge of the toroid also gains angular momentum in the nonlinear toroid. Despite this, the early nonlinear evolution and the linear predictions are almost in exact quantitative agreement.

Strong nonlinear effects, such as growth in the amplitude of higher m disturbances, $\mathcal{A}_m$, appear around $t = 2.5\ \tau_{max}$ when $\mathcal{A}_3 \approx 0.1$ and the QL torque, although very good at early times, will be less accurate around saturation because, as for the $T/|W| = 0.253$ toroid, nonlinear effects are more severe for the $T/|W| = 0.273$ toroid than they were for the $T/|W| = 0.192$ toroid (see discussion of $T/|W| = 0.253$ toroid). Consequently, although the self-interaction gravitational torque appears to play a role in saturation, we cannot argue that it is the dominant saturation mechanism as we did for the $m = 2$ I mode simulation discussed in §4.2.1. At $t \sim 3\ \tau_{max}$, $m = 3$ saturates with $\mathcal{A}_3 \approx 1.2$, and $T/|W|$ reaches its first minimum $T/|W| \sim 0.255$.[2] At saturation, the

[2] $\mathcal{A}_m$ can be greater than 1 using the definition of Pickett, Durisen, & Davis (1995). For the equilibrium toroid

toroid has filled-in and the outer radius of the toroid increased in size by more than 50 %. The toroid now more resembles a star with an extended Keplerian envelope rather than a disk at this time. Not surprisingly, the $m = 3$ eigenfunction no longer resembles the linear eigenfunction (see Figures 16 and 18). After saturation, the polytrope continues to expand as $T/|W|$ rebounds and reaches 0.284 at $t = 3.2\ \tau_{max}$ by which time the global oscillation in $m = 3$ is disrupted. After $t \sim 3.5\ \tau_{max}$, $\mathcal{A}_3$ continues to decline as $T/|W|$ oscillates in size. We halt the simulation at $t \sim 6\ \tau_{max}$. Although the polytrope has not yet stopped evolving, the simulation is ended because of poor energy conservation. The toroid showed no indication that continued dynamic evolution would lead to fission or fragmentation unless additional effects such as dissipation were introduced.

5. DISCUSSION

5.1. Comparison to Previous Works

Tohline & Hachisu (1990) and Woodward, Tohline, & Hachisu (1994) performed several simulations directly comparable to ours in their study of the properties of nonaxisymmetric gravito-rotation modes in self-gravitating toroids and star/disk systems. They performed a few simulations of self-gravitating toroids for $n = 3/2$ and $q = 3/2$, 7/4, or 2 using a fully nonlinear, three-dimensional, numerical hydrodynamics computer code using seven selected models to sample parameter space. They, however, only considered even m modes. Our results, where they overlap with the even-m I mode results given in Woodward, Tohline, & Hachisu (1994), agree very well.[3] The ω_2 are within 5 % and the τ_2 within 5-10 % for the I modes. Our eigenvalues don't agree well with the one J mode simulation presented in Woodward, Tohline, & Hachisu (1994), the $T/|W| = 0.27$ toroid model for which they missed the fastest growing mode, the $m = 3$ mode, because they modeled only even m modes.

A more extensive study of self-gravitating toroids was performed by Andalib, Tohline, & Christodoulou (1997) who studied P, I, and J modes in narrow, incompressible, self-gravitating annuli with constant specific angular momentum and circular meridional cross-sections. The set of assumptions forms the *ICT* approximation. Although not directly comparable to our work because of these simplifying assumptions, *ICT* studies offer an useful framework for a discussion of our study of the stability properties of self-gravitating toroids. Andalib, Tohline, & Christodoulou (1997) present stability conditions using $T/|W|$ as the stability parameter (see their Figures 6 and 7 for I modes and Figures 10 and 11 for J modes). (i) For the I modes, Andalib, Tohline, and

---

and the linear eigenfunction, $\mathcal{A}_2$ $1.2\int |\delta\rho| \mathrm{d}^3\mathrm{x}$.

[3]The Woodward, Tohline, & Hachisu (1994) calculations were performed using a nonlinear hydrodynamics computer code. So, strictly speaking, they were never in the linear regime. Linear in the context of the nonlinear simulations of Woodward, Tohline, & Hachisu means the portion of the evolution where exponential growth was observed.

Christodoulou (1997) found that $m = 1$ modes were the most unstable, instability setting in for $T/|W| > 0.176$. The $m = 2$ modes were less unstable, instability setting in for $T/|W| > 0.262$. (ii) For the J modes, Andalib, Tohline, and Christodoulou found that the $m = 4$ and 5 modes were the most unstable with instability setting in for $T/|W| > 0.302$. Other $m > 2$ J modes became unstable only for higher $T/|W|$.

Our results are in qualitative agreement with those of Andalib, Tohline, & Christodoulou (1997) despite the fact that the toroids used in our study populate a regime in parameter space where the ICT assumptions are the most suspect. ICT results are the most accurate for toroids with small aspect ratio, $\epsilon \ll 1$. For toroids with $T/|W| < 0.27$, $\epsilon > 0.3$-0.4. For I modes, we find that the $m = 2$ barlike modes are the most unstable with instability setting in for $T/|W| >$ 0.16-0.18, and that $m = 1$ I modes are generally more stable, strong instability setting in at $T/|W|$ ~ 0.22. For J modes, we find that $m = 2$, 3, and 4 modes are unstable for $T/|W| > 0.25$-0.26. Instability (i) sets in at lower $T/|W|$ for both I and J modes, (ii) sets in at higher m for I modes, and (iii) sets in at lower m for J modes than found by Andalib, Tohline, & Christodoulou. These differences likely arise from breakdowns in the assumptions which underlie the ICT model. Near instability thresholds, toroids are wide and the ICT theory breaks down. The breakdown likely affects low m modes more strongly than high m modes. This is because low m modes have longer wavelengths than high m modes. Studies of uniformly rotating incompressible fluids find that nonaxisymmetric modes with $l = |m|$ are the most unstable for given m. Here, l (and m) are the angular quantum numbers of the associated Legendre polynomials. Consequently, low m modes will have long wavelengths in the meridional plane as well as in azimuthal direction. The accuracy of their modeling then strongly depends on how well the surface of the toroid is resolved. The accuracy of the high m modes, with their shorter wavelengths, relies more on the accurate modeling of the interior volume of the toroid. If results from the two calculations are to differ then, they will most likely differ for low m modes near threshold which is where we find the discrepancies. Overall, the results of our exact calculations of the properties of the I and J modes in self-gravitating toroids and those from ICT studies, although not in quantitative agreement, exhibit good qualitative agreement and ICTs are useful tools for the study of the nonaxisymmetric modes of even wide self-gravitating disks.

The location of the instability thresholds for toroids are well-defined in terms of $T/|W|$, they, however, do not depend as cleanly on other stability parameters used in ICT studies. (i) We find that the location of I mode instability thresholds vary strongly with ϵ, the width of the toroid (see Table 1), $\epsilon \approx 0.91$, 0.64, and 0.55 at the $m = 2$ instability thresholds for $q = 1$, 3/2, and 2 toroids. (ii) We find that the locations of the instability thresholds in terms of the self-gravity parameter, p, where p is given by $p^2 = 4\pi G\rho_{max}/\Omega^2_{max}$ are consistent with those presented in Andalib, Tohline, & Christodoulou, but with some significant differences, the I mode instability thresholds fall at $p = 2.7$, 2.7, and 3.5 for toroids with $q = 1$, 3/2, and 2, and that J modes dominate I modes when $p > 4.6$, 5.2, and 5.7 for toroids with $q = 1$, 3/2, and 2. Andalib, Tohline, & Christodoulou (1997) found that I modes are unstable for $p > 2.97$, in good agreement with

our results, but that J modes are unstable for $p > 5.205$ and dominate I modes when $p > 7.526$, similar to our results. The predictions of Andalib, Tohline, & Christodoulou (1997) are most useful when given in $T/|W|$-space for toroids, although they are reasonably good when p is used. They are least useful when given in terms of ϵ.

Toroids are susceptible to I and J modes in the linear regime, depending on the $T/|W|$ of the toroid but, *How does instability ultimately manifest itself?* We follow the evolution of unstable toroids into the nonlinear regime. Our simulations follow behavior predicted by our linear and QL analyses at early times. At long times, we find that toroids do not undergo prompt fission as a result of the development of I mode instabilities (*cf.*, Tohline & Hachisu 1990, Woodward, Tohline, & Hachisu 1994) or J mode instabilities. The ultimate outcome of I mode and J mode instabilities appears to be quasi-stable, damping slightly nonaxisymmetric figures, barlike in the unstable I mode regime or a higher order figure in the unstable J mode regime. Further evolution of the toroids will then be driven by dissipative processes such as radiative cooling or viscosity (see Lebovitz 1987).

5.2. Protostellar Star/Disk Systems

Low mass star formation occurs in cold, overdense regions in Giant Molecular Clouds (GMCs) (for a recent of star formation, see McKee & Ostriker 2007). Cold cloud cores contain 1 to 2 $M_\odot$ and have large specific angular momenta, specific angular momenta much larger than found in any star in the Galaxy (*e.g.,* see Tohline 2002). Cloud cores are typically evolved in the sense that they are centrally condensed. If the initial cloud cores are near the local Jeans mass, then their collapse likely leads to the formation of a star/disk system rather than to a single star (*e.g.,* see Tohline 2002). For uniform density cloud cores which start in uniform rotation, a small equilibrium object first forms from cloud material with low specific angular momentum, the material which was initially close to the rotation axis of the cloud. Later, material farther from the rotation axis with larger specific angular momentum flows inward, but is unable to accrete onto the central object. The material forms a circumstellar disk which slowly increases in mass and size with time. The central core generally contains less than a few percent of the total cloud mass under typical conditions (Shu, Adams, & Lizano 1987). The system evolves as the circumstellar disk continues to accrete, growing in mass as the central core more or less remains at its original mass. The formation of stellar-sized objects is then determined by how the mass contained in the disk finds its way onto the central core. A plausible transfer mechanism is the development of gravito-rotation driven nonaxisymmetric instabilities in the disk. Such instabilities may arise as the disk mass accretes and grows. Studies of star/disk systems which do not include the effects of accretion find that instability sets in when M_*/M_d falls below $\sim$ 0.1-1 (*e.g.,* Tohline 2002).

The work of Andalib, Tohline, & Christodoulou (1997) suggests that toroids represent the limit of star/disk systems when the mass of the central star goes to zero; they do not form a set of singular disk solutions. If this is correct, then results from our simulations of instabilities in toroids

offer insight into the stability properties of protostellar systems at late times when massive disks have formed around small, centrally condensed cores, systems where the central mass compared to the disk mass $M_*/M_d \ll 1$ (Shu, Adams, & Lizano 1987) or to the case of the circumstellar disks which form around massive protostars (Cesaroni *et al.* 2007). This question is currently under investigation in the extensive parameter space study of Hadley *et al.* (2010). Preliminary results from a simulation of star/disk system with an $(n, q) = (3/2,3/2)$ disk, $M_*/M_d = 0.05$, and $R_-/R_+ = 0.173$ ($T/|W| = 0.219$, $R_+ = 4.97$, $j = 0.766$, $\rho_{max} = 0.0123$, $R_{max} = 2.360$, $\tau_{max} = 49.4$), to be fully discussed in Hadley *et al.* (2010) are presented here. The system shows an unstable $m = 2$ barlike I mode with $(\omega_2/\tau_{max}, \tau_2^{-1}\tau_{max}) =$ (-1.035,2.38), $R_\phi = 1.66$, $R_\lambda = 3.16$ whose density eigenfunction is shown in Figure 19. The star/disk system's unstable barlike mode is similar to that of the (3/2,3/2) toroid with the same aspect ratio, $R_-/R_+ = 0.173$. The $m = 1$ mode complicates the discussion as it shows different behavior. Toroids show two $m = 1$ modes with eigenvalues $(\omega_1/\tau_{max}, \tau_1^{-1}\tau_{max}) =$ (-2.04,0.101) and (,). The $m = 1$ mode in the star/disk system dominates the barlike mode with $(\omega_1/\Omega_{max}, \tau_1^{-1}\tau_{max}) =$ (-0.871,3.065). This difference is due to the inclusion of the low mass central star and allowing it to move in response to disk perturbations (see Adams, Ruden, & Shu 1989, Noh, Vishniac, & Cochran 1992, Taga & Iye 1998). In a test calculation in which the position of the central star was fixed, the $m = 1$ mode only grew weakly, as in the toroid simulation. So, although the $m \geq 2$ modes for this toroid are the limiting forms for those of low star mass star/disk systems, the $m = 1$ modes of toroids are not for this small aspect ratio system.

Toroids with the specific angular momentum distribution of a Maclaurin spheroid may form through the collapse of nearly uniform density rotating cloud cores whose mass is significantly larger than the local Jeans mass (*e.g.*, see Tohline 2002). Hachisu, Tohline, & Eriguchi (1987) investigated this scenario in (F,$T/|W|$)-space where F is a parameter formed from G, K, j, and M. F is conveniently expressed in terms of the initial ratios of the thermal energy to the gravitational energy of the cloud, $\alpha_\circ$, and the rotational kinetic energy to the gravitational energy of the cloud, $\beta_\circ$, as

$$\mathrm{F} = 1.049\alpha_\circ^{0.6}\beta_\circ^{-0.143} \tag{42}$$

for an $n = 1.5$ gas cloud. Clouds whose masses are greater than the local Jeans mass have $\alpha_\circ \ll 1/2$. Such cold clouds are expected to collapse homologously with constant F and increasing $\beta = T/|W|$. Along a smooth sequence of collapsing spheroids, the barlike mode has a bifurcation point at $T/|W| \approx 0.27$ (*e.g.*, Tassoul 1978) and the ring-like sequence forms at $T/|W| \approx 0.41$. Numerical simulations found, however, that when spheroids were able to bypass the barlike bifurcation point, they became unstable to ring formation at $T/|W| \approx 0.39$, not $T/|W| = 0.41$. This seeming discrepancy arose because the $T/|W|$ for the ring-like sequence is not a single-valued function of the angular momentum j. Two distinct equilibria are possible except when $j \approx 2.86$ and $T/|W| \approx 0.39$ where the two branches merge (see Figure 1 in Hachisu, Tohline, & Eriguchi 1987). Hachisu, Tohline, & Eriguchi (1987) argued that collapsing clouds would evolve from low-to-high $T/|W|$ and eventually settle into the lowest available $T/|W|$ equilibrium. For small F (large j), they argued that condensed core collapses would approach Maclaurin-like toroidal equilibria rather

than spheroidal equilibria. We calculated structures and then determined the stability properties of several Maclaurin-like toroids. Our results are summarized in Tables 4 & 5 where we give properties of equilibrium toroids from both branches and the eigenvalues from our linear analyses of selected equilibrium models.

We show the density structure in a meridional cross-section and Ω for the Maclaurin-like toroid with $R_-/R_+ = 0.176$, $j = 2.90$, and $T/|W| = 0.384$ in Figure 20. The toroid is much flatter than power law toroids with the same R_-/R_+. As for the toroids with power law Ω, the density maximum falls in the interior of the toroid, $R_{max} \sim 0.3\ R_{max}$. However, unlike for the toroids with power law Ω, the angular velocity distribution is not monotonic. Ω reaches a peak at ~ 0.4 R_{max} a little outside the location of the density maximum. The toroid shows a narrow ring-like structure where Ω increases with radius outside of which lies an extended disk-like structure. In the disk-like region, Ω falls off as ϖ^{-1}. We show the $m = 1$, 2, and 3 eigenfunctions for this model in Figure 21. The modes are all strongly unstable with $m = 2$ the fastest growing mode. The $|\delta\rho|/\rho_\circ$ eigenfunction reaches maxima at the inner and outer edges of the toroid with a π/m phase shift at $\sim R_{max}$. For larger j toroids, the eigenfunction structures are similar but the rapid phase shift moves to radii smaller than R_{max}. No Maclaurin-like toroid tested was stable so that Maclaurin-like toroids can, at best, serve only as metastable equilibria in the cloud collapse process.

6. CONCLUSIONS

We investigated the dynamic nonaxisymmetric instabilities of thick, self-gravitating, inviscid polytropic toroids using linear, quasi-linear, and nonlinear modeling techniques. Our survey covered a much larger portion of parameter space than did previous workers. The results of our simulations agree well with earlier calculations where they directly overlap, but differ significantly in cases where our models left the regimes where the assumptions which underlie the earlier works were the most suspect. Self-gravitating toroids are susceptible to a broad range of gravito-rotation nonaxisymmetric instabilities. For polytropic toroids with power law angular velocity distributions, we find that for nonaxisymmetric modes with azimuthal dependence $e^{im\phi}$, where m is the azimuthal mode number and ϕ is the azimuthal angle, that instability sets in through $m = 2$ I modes at $T/|W| \sim$ 0.16-0.18, where T is the rotational kinetic energy and W is the gravitational energy. Instability in the $m = 2$ I mode peaks in strength around $T/|W| =$ 0.22-0.23 and then weakens. For toroids with polytropic index $n = 3/2$ and power law angular velocity distributions with indices $q = 3/2$ and 2, the $m = 2$ I mode becomes stable at $T/|W| \sim$ 0.26. Just before the $m = 2$ mode stabilizes, an $m = 1$ I mode instability sets in and is expected to dominate the $m = 2$ mode for $T/|W| \gtrsim 0.25$. However, around the $T/|W|$ where the $m = 1$ mode starts to dominate the $m = 2$ I mode, J modes appear. J modes with $m = 2$, 3, and 4 become unstable for $T/|W| \sim$ 0.25-0.26, 0.23-0.25, and 0.25-0.26, respectively, $m \geq 3$ J modes quickly dominate the $m = 1$ I mode and are expected to control the evolution of toroids with $T/|W| \gtrsim$

0.26. Toroids are thus susceptible to I and J modes in the linear regime, depending on the $T/|W|$ of the toroid. However, we find that toroids do not undergo prompt fission as a result of the development of either I or J mode instabilities into the nonlinear regime. The ultimate outcome of I and J mode instabilities appears to be quasi-stable, damping nonaxisymmetric figures with off-center maxima, either barlike in form for the I modes or tri-cornered or square figures for the J modes. Consequently, the further evolution of such figures driven by cooling may lead to the onset of elliptical instabilities and eventually to fission in the scenario first described in Lebovitz 1987 (see also, Lebovitz & Lifschitz 1996, Cazes & Tohline 2000, Ou & Tohline 2007).

The authors thank the National Science Foundation and the National Aeronautics and Space Administration for their support during the course of this research.

REFERENCES

Adams, F.C., Ruden S.P. & Shu F.H. 1989, Ap. J., 347, 959

Cesaroni, R., Galli, D., Lodato, G., Walmsley, C.M., & Zhang, Q. 2007, arXiv:astro-ph/0603093v1

Andalib, S.W., Tohline, J.E., & Christodoulou, D.M. 1997, Ap. J. S., 108, 471

Cazes, J. E. & Tohline, J.E. 2000, Ap. J., 532, 1051

Eriguchi, Y. & Hachisu, I. 1983, Progr. Theor. Phys., 69, 1131

Goodman, J. & Narayan, R. 1988, M.N.R.A.S., 231, 97

Hachisu, I. 1986 Ap. J. Suppl., 61, 479

Hachisu, I. & Eriguchi, Y. 1982, Progr. Theor. Phys., 68, 206

Hachisu, I. & Eriguchi, Y. 1983, Ap. & S.S., 99, 71

Hachisu, I. & Eriguchi, Y. 1985, As. Sp. Sci., 99, 71

Hachisu, I., Tohline, J., & Eriguchi, Y. 1987, Ap. J., 323, 592

_____. 1988, Ap. J. Suppl., 66. 315

Imamura, J.N., Durisen, R.H., & Pickett, B.K. 2000, Ap. J., 528, 946

Imamura, J.N., Toman, J., Durisen, R. H., Pickett, B., K., & Yang, S. 1995, Ap. J., 444, 363

Kojima, Y. 1986, Progr. Theor. Phys., 75, 251

Kojima, Y. 1989, M. N. R. A. S., 236, 589

Lebovitz, N.R. 1987, Highlights of Astronomy, Vol. 8, ed. C. McNally, (Boston: Kluwer), 129

Lebovitz, N.R. & Lifschitz, A. 1996, Ap. J., 458, 699

Lin, D.N.C. & Papaloizou, J.C.B. 1995, Ann. Rev. Astr. As., 33, 505

_____. 1996, Ann. Rev. Astr. As., 34,

McKee, C.F. & Ostriker, E.C. 2007, Ann. Rev. As. Astr., 45, 565

Nakagawa, Y. & Sekiya, M. 1992, M.N.R.A.S., 256, 685

Noh, H., Vishniac, E.T., & Cochran, W.D. 1992, Ap J, 397, 347

Ou, S., Tohline, J.E., & Motl, P.M. 2007, Ap. J., 665, 1074

Papaloizou, J.C. & Savonije, G.J. 1991, A. & A., 248, 353

Papaloizou, J.C. & Pringle, J.E. 1984, M.N.R.A.S., 208, 702

Pickett, B.K., Durisen, R. H., & Davis, G.A. 1996, Ap. J., 458, 714

Taga, M. & Iye, M. 1998, Ap J, 299, 1132

Shu, F.H,, Adams, D.C., & Lizano, S. 1987, Ann. Rev. Astr. As., 25, 23

Tassoul, J.-L. 1978, Theory of Rotating Stars (Princeton U. Press)

Tohline, J.E. 2002, Ann. Rev. As. Astr., 40, 349

Tohline, J.E., Durisen, R.H., & McCollough, M. 1985, Ap. J., 298, 220

Tohline, J.E., & Hachisu, I. 1990, Ap. J., 361, 394

Toman, J., Imamura, J.N., Pickett, B.K., & Durisen, R.H. 1998, Ap. J., 497, 370

Williams, H.A. & Tohline, J.E. 1987, Ap. J., 315, 594

Wong, C.-Y. 1974, Ap. J., 190, 675

Woodward, J.W., Tohline, J.E., & Hachisu, I. 1994, Ap. J., 420, 247

This preprint was prepared with the AAS LaTeX macros v4.0.

Table 1. $(n, q) = (3/2,1)$ Equilibrium Models

$\frac{T}{\|W\|}$	ρ_{max}	τ_{max}	R_{max}	j	$\frac{R_-}{R_+}$	R_+	ϵ
0.153	0.0211	35.30	1.556	0.489	0.115	3.961	0.708
0.162	0.0189	38.71	1.697	0.524	0.126	4.136	0.692
0.168	0.0175	40.87	1.787	0.547	0.134	4.254	0.681
0.173	0.0163	43.44	1.889	0.570	0.142	4.373	0.671
0.178	0.0153	45.85	1.985	0.593	0.150	4.494	0.661
0.181	0.0145	47.51	2.052	0.610	0.156	4.585	0.652
0.182	0.0143	48.08	2.075	0.616	0.158	4.616	0.649
0.187	0.0133	50.74	2.177	0.639	0.166	4.740	0.640
0.191	0.0125	53.55	2.283	0.662	0.173	4.865	0.630
0.205	0.0101	63.58	2.652	0.743	0.201	5.320	0.597
0.215	0.00844	73.21	2.992	0.813	0.224	5.731	0.570
0.230	0.00648	90.39	3.569	0.927	0.262	6.427	0.529
0.238	0.00552	103.35	3.981	1.001	0.285	6.901	0.506
0.243	0.00497	112.21	4.258	1.052	0.301	7.233	0.489
0.253	0.00406	132.99	4.878	1.157	0.332	7.944	0.459
0.260	0.00343	152.43	5.437	1.250	0.358	8.589	0.434
0.260	0.00341	153.36	5.463	1.254	0.360	8.622	0.433
0.260	0.00339	154.20	5.486	1.257	0.360	8.640	0.433
0.261	0.00337	155.14	5.513	1.262	0.361	8.672	0.431
0.261	0.00332	156.93	5.562	1.269	0.363	8.723	0.430
0.262	0.00328	158.03	5.595	1.276	0.365	8.775	0.427
0.262	0.00324	159.86	5.645	1.283	0.367	8.826	0.426
0.263	0.00320	161.72	5.696	1.290	0.369	8.878	0.424
0.263	0.00316	163.60	5.747	1.298	0.371	8.931	0.423
0.266	0.00294	173.76	6.026	1.342	0.383	9.251	0.412
0.267	0.00287	177.03	6.116	1.357	0.387	9.361	0.408
0.268	0.00280	181.18	6.225	1.372	0.391	9.472	0.405
0.273	0.00248	200.79	6.744	1.449	0.410	10.051	0.388
0.276	0.00228	215.05	7.114	1.505	0.424	10.481	0.375
0.282	0.00192	248.14	7.945	1.623	0.452	11.408	0.352
0.293	0.00142	322.41	9.703	1.856	0.501	13.333	0.312
0.300	0.00113	391.01	11.231	2.046	0.536	14.989	0.285
0.303	0.00102	427.08	12.004	2.138	0.551	15.814	0.274
0.313	0.00074	566.97	14.857	2.461	0.600	18.843	0.239
0.318	0.00065	641.14	16.236	2.609	0.621	20.290	0.224
0.323	0.00057	722.21	17.786	2.770	0.640	21.905	0.212
0.328	0.00049	813.14	19.492	2.948	0.660	23.720	0.196
0.334	0.00042	924.62	21.481	3.146	0.680	25.773	0.184
0.341	0.00036	1052.0	23.706	3.368	0.698	28.111	0.172

Table 2. $(n, q) = (3/2,3/2)$ Equilibrium Models

$\frac{T}{\|W\|}$	ρ_{max}	τ_{max}	R_{max}	j	$\frac{R_-}{R_+}$	R_+	ϵ
0.153	0.0211	35.30	1.556	0.489	0.115	3.961	0.708
0.162	0.0189	38.71	1.697	0.524	0.126	4.136	0.692
0.168	0.0175	40.87	1.787	0.547	0.134	4.254	0.681
0.173	0.0163	43.44	1.889	0.570	0.142	4.373	0.671
0.178	0.0153	45.85	1.985	0.593	0.150	4.494	0.661
0.181	0.0145	47.51	2.052	0.610	0.156	4.585	0.652
0.182	0.0143	48.08	2.075	0.616	0.158	4.616	0.649
0.187	0.0133	50.74	2.177	0.639	0.166	4.740	0.640
0.191	0.0125	53.55	2.283	0.662	0.173	4.865	0.630
0.205	0.0101	63.58	2.652	0.743	0.201	5.320	0.597
0.215	0.00844	73.21	2.992	0.813	0.224	5.731	0.570
0.230	0.00648	90.39	3.569	0.927	0.262	6.427	0.529
0.238	0.00552	103.35	3.981	1.001	0.285	6.901	0.506
0.243	0.00497	112.21	4.258	1.052	0.301	7.233	0.489
0.253	0.00406	132.99	4.878	1.157	0.332	7.944	0.459
0.260	0.00343	152.43	5.437	1.250	0.358	8.589	0.434
0.260	0.00341	153.36	5.463	1.254	0.360	8.622	0.433
0.260	0.00339	154.20	5.486	1.257	0.360	8.640	0.433
0.261	0.00337	155.14	5.513	1.262	0.361	8.672	0.431
0.261	0.00332	156.93	5.562	1.269	0.363	8.723	0.430
0.262	0.00328	158.03	5.595	1.276	0.365	8.775	0.427
0.262	0.00324	159.86	5.645	1.283	0.367	8.826	0.426
0.263	0.00320	161.72	5.696	1.290	0.369	8.878	0.424
0.263	0.00316	163.60	5.747	1.298	0.371	8.931	0.423
0.266	0.00294	173.76	6.026	1.342	0.383	9.251	0.412
0.267	0.00287	177.03	6.116	1.357	0.387	9.361	0.408
0.268	0.00280	181.18	6.225	1.372	0.391	9.472	0.405
0.273	0.00248	200.79	6.744	1.449	0.410	10.051	0.388
0.276	0.00228	215.05	7.114	1.505	0.424	10.481	0.375
0.282	0.00192	248.14	7.945	1.623	0.452	11.408	0.352
0.293	0.00142	322.41	9.703	1.856	0.501	13.333	0.312
0.300	0.00113	391.01	11.231	2.046	0.536	14.989	0.285
0.303	0.00102	427.08	12.004	2.138	0.551	15.814	0.274
0.313	0.00074	566.97	14.857	2.461	0.600	18.843	0.239
0.318	0.00065	641.14	16.236	2.609	0.621	20.290	0.224
0.323	0.00057	722.21	17.786	2.770	0.640	21.905	0.212
0.328	0.00049	813.14	19.492	2.948	0.660	23.720	0.196
0.334	0.00042	924.62	21.481	3.146	0.680	25.773	0.184
0.341	0.00036	1052.0	23.706	3.368	0.698	28.111	0.172

Table 3. $(n, q) = (3/2,2)$ Equilibrium Models

$\frac{T}{\|W\|}$	ρ_{max}	τ_{max}	R_{max}	j	$\frac{R_-}{R_+}$	R_+	ϵ
0.162	0.0173	44.35	1.909	0.516	0.197	4.228	0.564
0.172	0.0149	49.96	2.127	0.569	0.215	4.495	0.547
0.180	0.0133	55.08	2.314	0.611	0.228	4.715	0.535
0.192	0.0111	63.25	2.613	0.678	0.250	5.081	0.514
0.203	0.00930	72.26	2.933	0.748	0.271	5.474	0.494
0.216	0.00749	85.86	3.389	0.841	0.299	6.018	0.470
0.221	0.00684	92.52	3.603	0.882	0.310	6.267	0.460
0.231	0.00563	107.47	4.081	0.974	0.336	6.842	0.437
0.236	0.00508	116.67	4.363	1.025	0.350	7.174	0.425
0.244	0.00439	131.67	4.804	1.101	0.369	7.676	0.410
0.250	0.00380	147.80	5.270	1.180	0.389	8.214	0.394
0.263	0.00286	185.84	6.316	1.349	0.428	9.415	0.362
0.265	0.00275	192.14	6.485	1.375	0.434	9.611	0.357
0.276	0.00208	242.96	7.774	1.563	0.473	11.039	0.328
0.289	0.00143	332.48	9.892	1.849	0.526	13.377	0.289
0.300	0.00103	438.16	12.193	2.132	0.571	15.858	0.257
0.309	0.00081	538.50	14.256	2.371	0.604	18.082	0.234
0.321	0.00057	729.87	17.941	2.771	0.651	21.990	0.202

Table 4. Equilibrium Models: Maclaurin Sequences

$T/\|W\|$	ρ_{max}	Ω_{max}	R_{max}	j	R_-/R_+	R_+	ϵ
0.407	2.25×10^{-4}	0.00816	10.6	3.01	0.008	55.2	0.958
0.406	2.27×10^{-4}	0.00859	11.0	3.00	0.016	54.9	0.920
0.403	2.47×10^{-4}	0.00831	11.0	2.94	0.048	52.8	0.770
0.398	2.70×10^{-4}	0.00875	11.4	2.88	0.080	50.7	0.356
0.394	2.83×10^{-4}	0.00774	12.5	2.85	0.110	48.4	0.453
0.389	2.89×10^{-4}	0.00719	13.6	2.89	0.144	48.5	0.529
0.385	2.84×10^{-4}	0.00645	15.1	2.90	0.177	49.8	0.573
0.381	2.70×10^{-4}	0.00554	17.0	2.98	0.209	52.3	0.643
0.378	2.47×10^{-4}	0.00465	19.4	3.10	0.240	56.3	0.697
0.374	2.16×10^{-4}	0.00384	22.9	3.28	0.272	62.9	0.747
0.371	1.76×10^{-4}	0.00314	28.6	3.59	0.303	74.5	0.826

Table 5. Eigenvalues: Maclaurin Sequences

R_-/R_+	$T/\|W\|$	$m=1$	$m=2$	$m=3$
0.110	0.349	-1.122,0.493	-1.231,0.661	-2.563,0.683
0.144	0.394	-1.138,0.517	-1.260,0.696	-2.611,0.667
0.178	0.384	-1.207,0.565	-1.427,0.797	-2.801,0.665
0.209	0.381	-1.233,0.578	-1.397,0.784	-2.863,0.628
0.240	0.378	-1.245,0.642	-1.509,0.841	-2.070,0.725
0.272	0.374	-1.216,0.678	-1.609,0.939	-2.149,0.907
0.303	0.371	-1.214,0.682	-1.633,0.952	-2.112,1.014

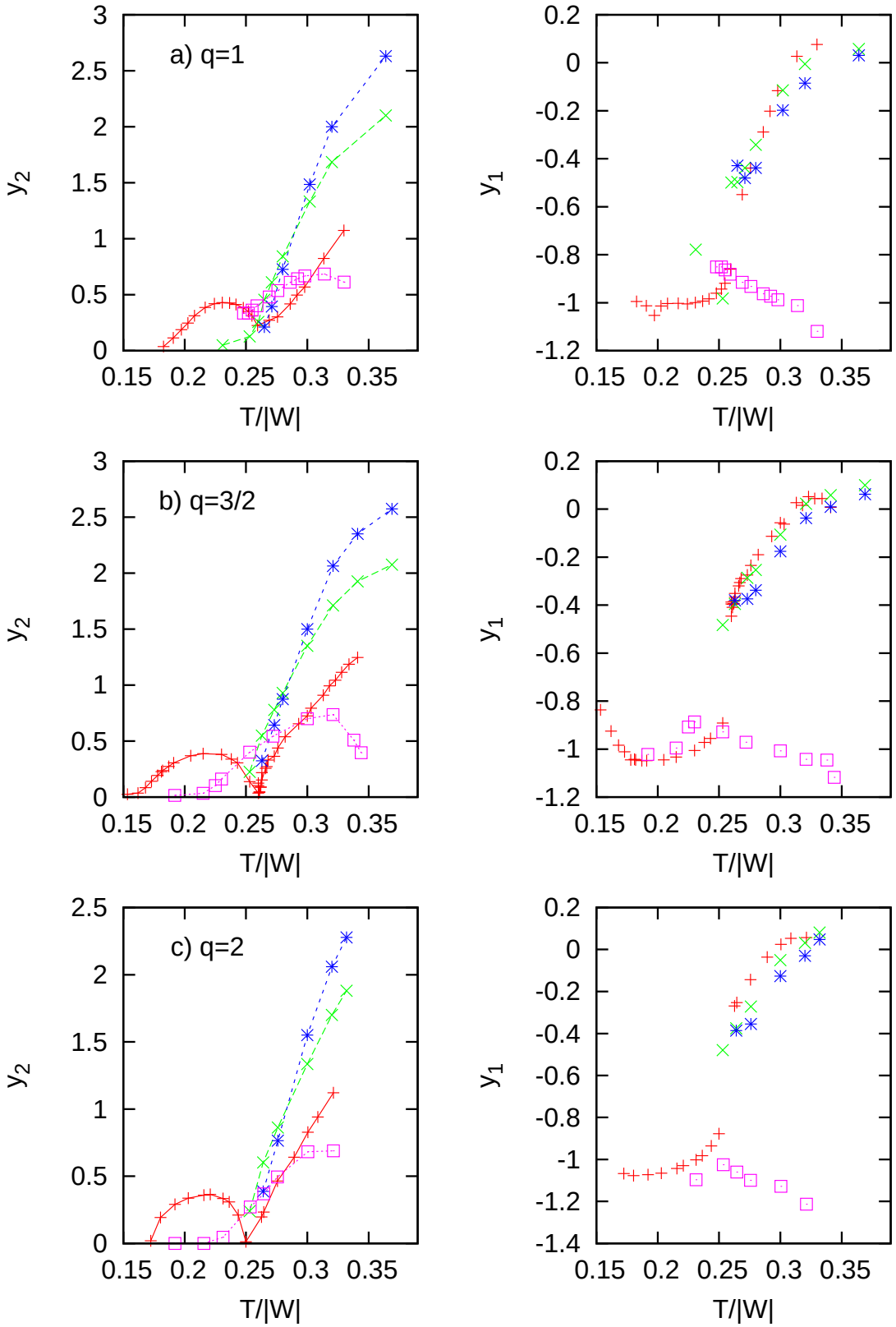

Fig. 1.— Low m eigenvalues for toroids with $q = 1$, 3/2, and 2. The left column shows y_2, the growth rates, and the right column shows y_1, the oscillation frequencies. The squares with a dot are for $m = 1$, "+" are for $m = 2$, the "×" are for $m = 3$, and the "∗" are for $m = 4$. The $m = 1$ oscillation eigenvalues plotted are -y_2 because corotation falls between ρ_{max} and the inner edge of the disk.

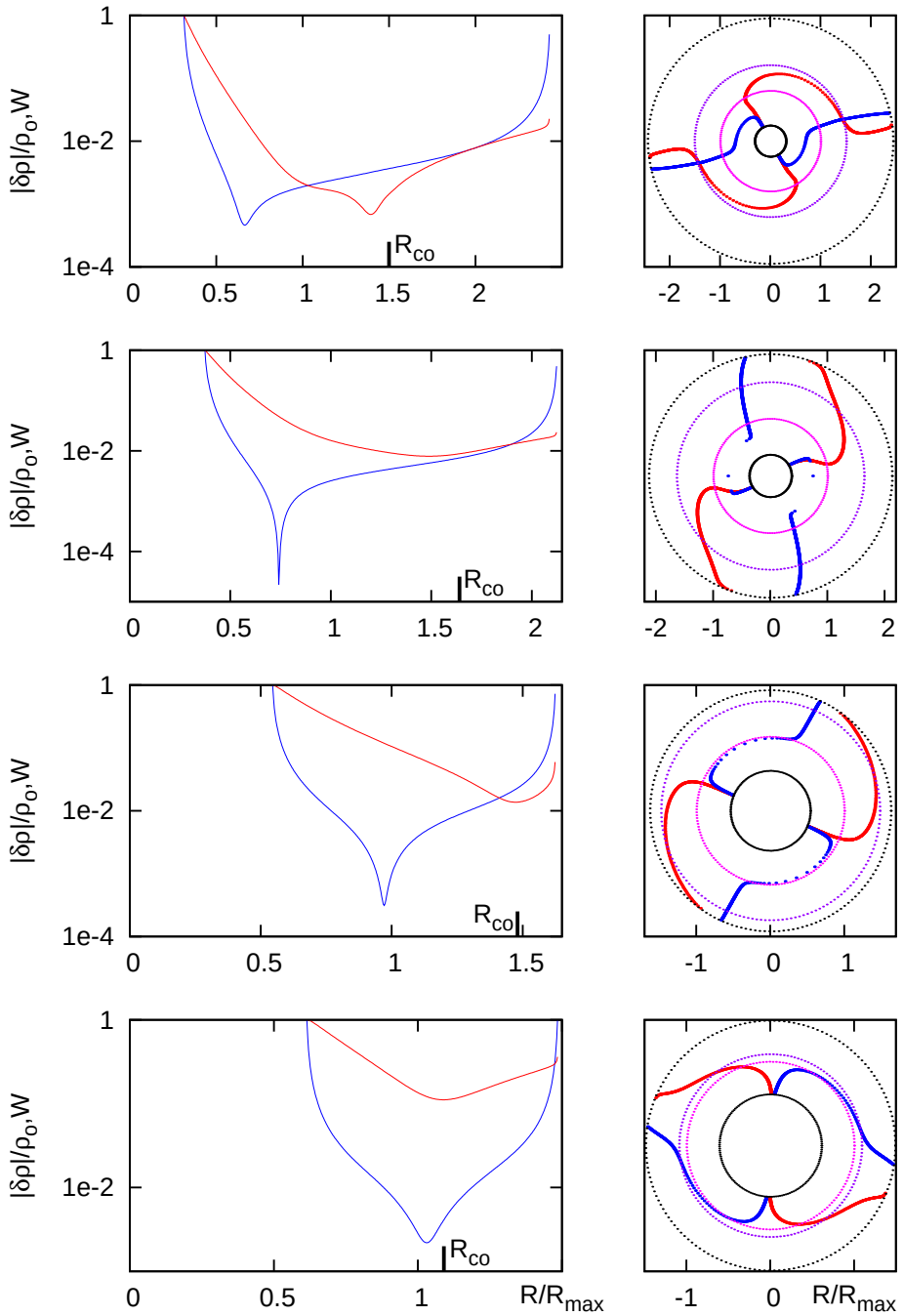

Fig. 2.— The $m = 2$ mode eigenfunctions and constant phase loci in the equatorial plane for the $(n, q) = (3/2,3/2)$, $T/|W| = 0.163$, 0.192, 0.253, and 0.273 toroids from top-to-bottom. The red lines are $|\delta\rho|/\rho_\circ$ and the green lines are $\mathcal{W}$. The three circles in the phase plots (right hand panels) mark the inner and outer radii of the toroid and the location of ρ_{max}.

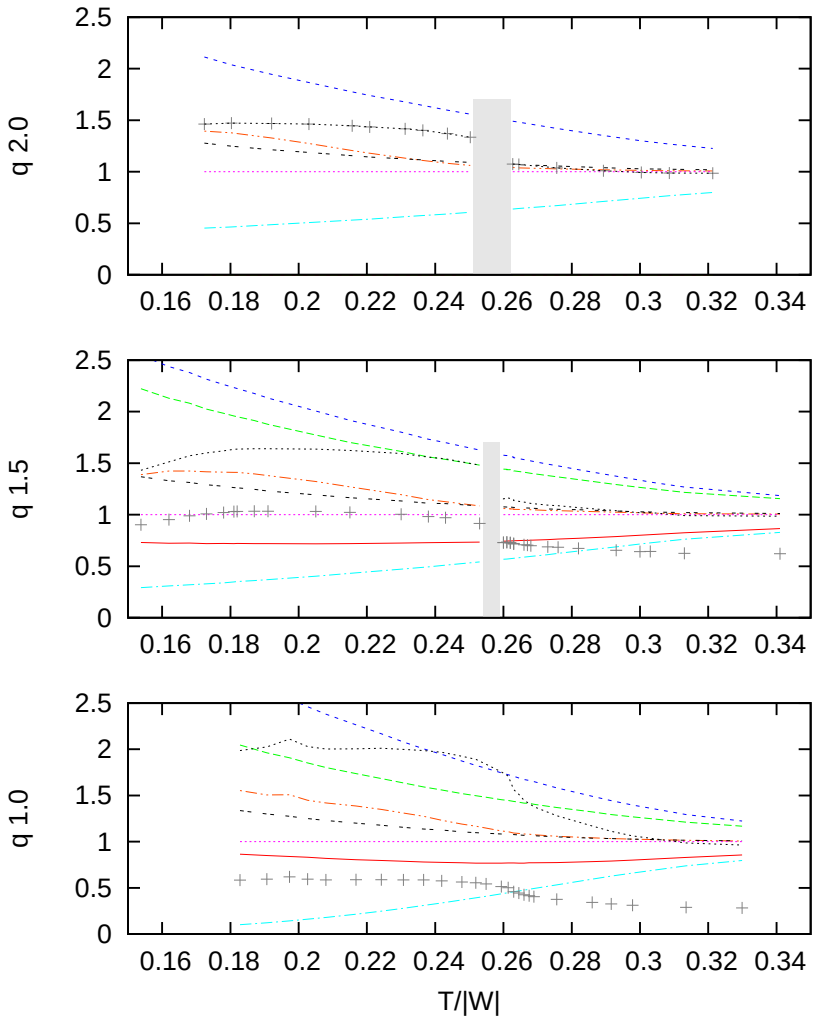

Fig. 3.— Critical radii for the $m = 2$ barlike modes for the $(n, q) = (3/2,2)$, $(3/2,3/2)$, and $(3/2,1)$ toroid sequences from top-to-bottom. The radii are in units of R_{max}. The dashed-dotted lines (red) mark R_γ, the short-dotted (blue) and long-dotted (aqua) lines mark R_+ and R_-, respectively, the solid (red) and medium-dashed (green) lines mark Q_- and Q_+, respectively, the short-dashed (magenta) lines mark R_{max}, the crosses (black) mark R_{ILR}, the double-dash-space (black) lines mark R_λ, and the short-dashed (black) lines mark R_{co}. The grey boxes in the top two panels marks the I to J mode transition regions.

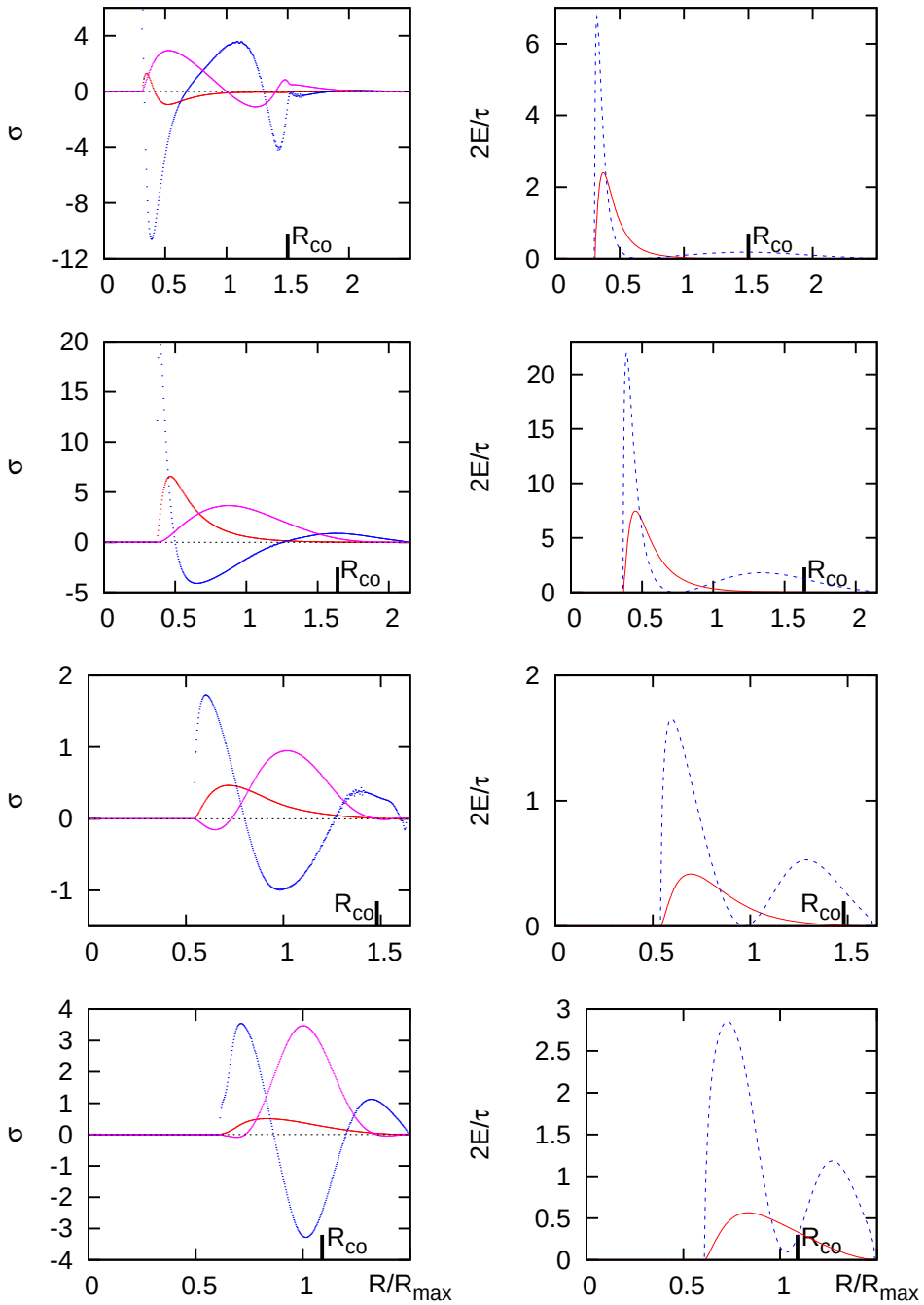

Fig. 4.— The time rate of change of the perturbed energies, $2\left\langle \mathcal{E}\right\rangle_k/\tau$ and $2\left\langle \mathcal{E}\right\rangle_h/\tau$ and, the stresses, σ_R, σ_Π, and σ_Φ for the $m = 2$ modes of the (n,q) = (3/2,3/2), $T/|W| = 0.163$, 0.192, 0.253, and 0.273 toroids, from top-to-bottom. The stresses are scaled in units of $0.5|W|/(V\tau_{max})$ where V is the volume of the toroid) and the time rate of change of the perturbed energies are scaled in units of $0.5|W|/\tau_{max}$. The left hand panels show the stresses, σ_R (solid lines), σ_Φ (dashed lines), and σ_π (dotted lines) and the right hand panels show the growth rates of the energies $2\mathcal{E}_k/\tau$ (solid lines), and $2\mathcal{E}_h/\tau$ (dashed lines). The stresses and perturbed energies are calculated using linear eigenfunctions normalized so that $\int |\delta\rho| \mathrm{d}^3\mathrm{x} = 1$.

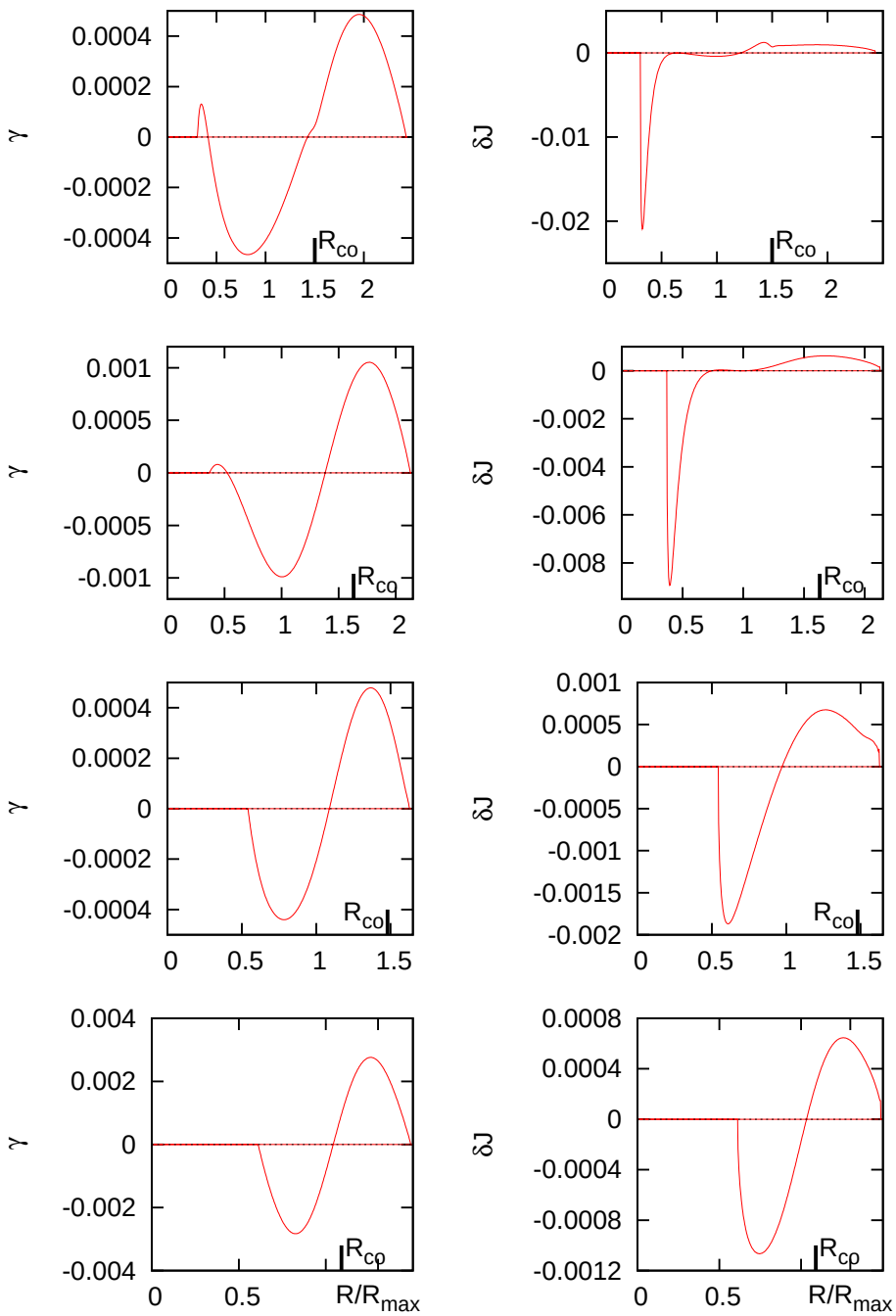

Fig. 5.— The self-interaction gravitational torque γ (left hand panels) and the time-averaged angular momentum of the perturbed modes δJ (right hand panels) for the (n,q) = (3/2,3/2), $T/|W| = 0.163$, 0.192, 0.253, and 0.273 toroids, from top-to-bottom. The γ are scaled in units of j/τ_{max}. The γ and δJ are calculated using linear eigenfunctions normalized so that $\int |\delta\rho| \mathrm{d}^3\mathrm{x} = 1$.

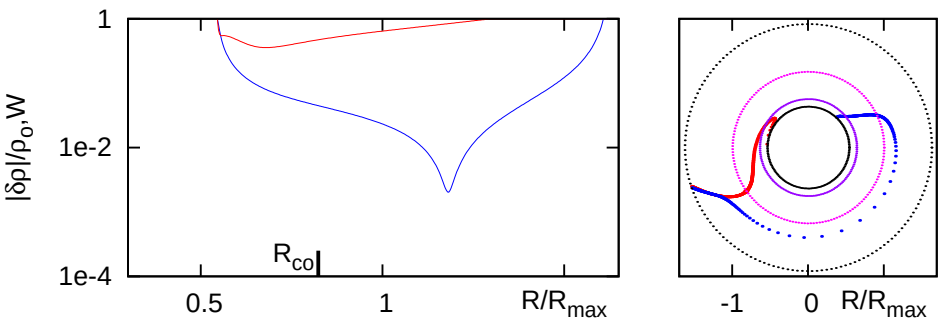

Fig. 6.— The $m = 1$ mode eigenfunction and properties for the $(n, q) = (3/2{,}3/2)$, $T/|W| = 0.253$ toroid. The eigenfunctions and constant phase loci in the equatorial plane are shown. The red lines are $|\delta\rho|/\rho_\circ$ and the green lines are $\mathcal{W}$. The three circles in the phase plot (right hand panel) mark the inner and outer radii of the toroid and the location of ρ_{max}.

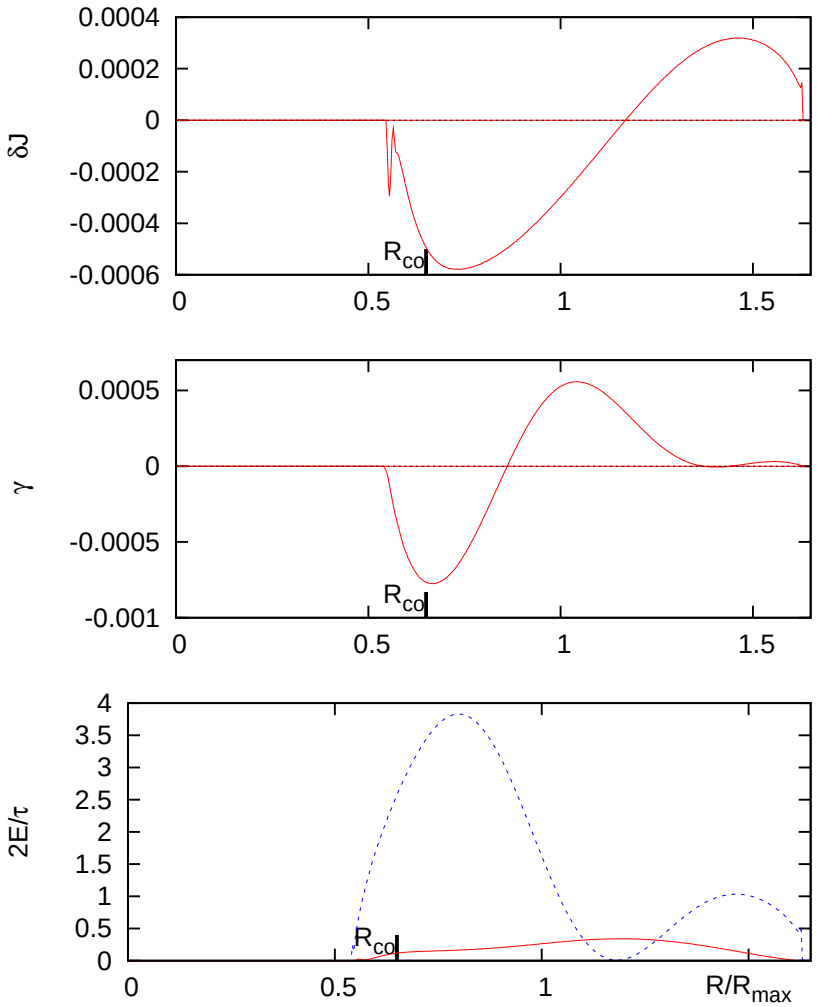

Fig. 7.— The $m = 1$ mode eigenfunction properties for the $(n, q) = (3/2,3/2)$, $T/|W| = 0.253$ toroid. The self-interaction gravitational torque γ, the time-averaged angular momentum of the perturbed mode δJ, and the perturbed energy growth rates $2\mathcal{E}_h/\tau$ and $2\mathcal{E}_k/\tau$ are shown. The perturbed energies are scaled in units of the total energy of the toroid, $0.5|W|$, divided by τ_{max}, and γ is scaled in units of j/τ_{max}. The δJ, γ, and perturbed energies are calculated using linear eigenfunctions normalized so that $\int |\delta\rho| \mathrm{d}^3\mathrm{x} = 1$.

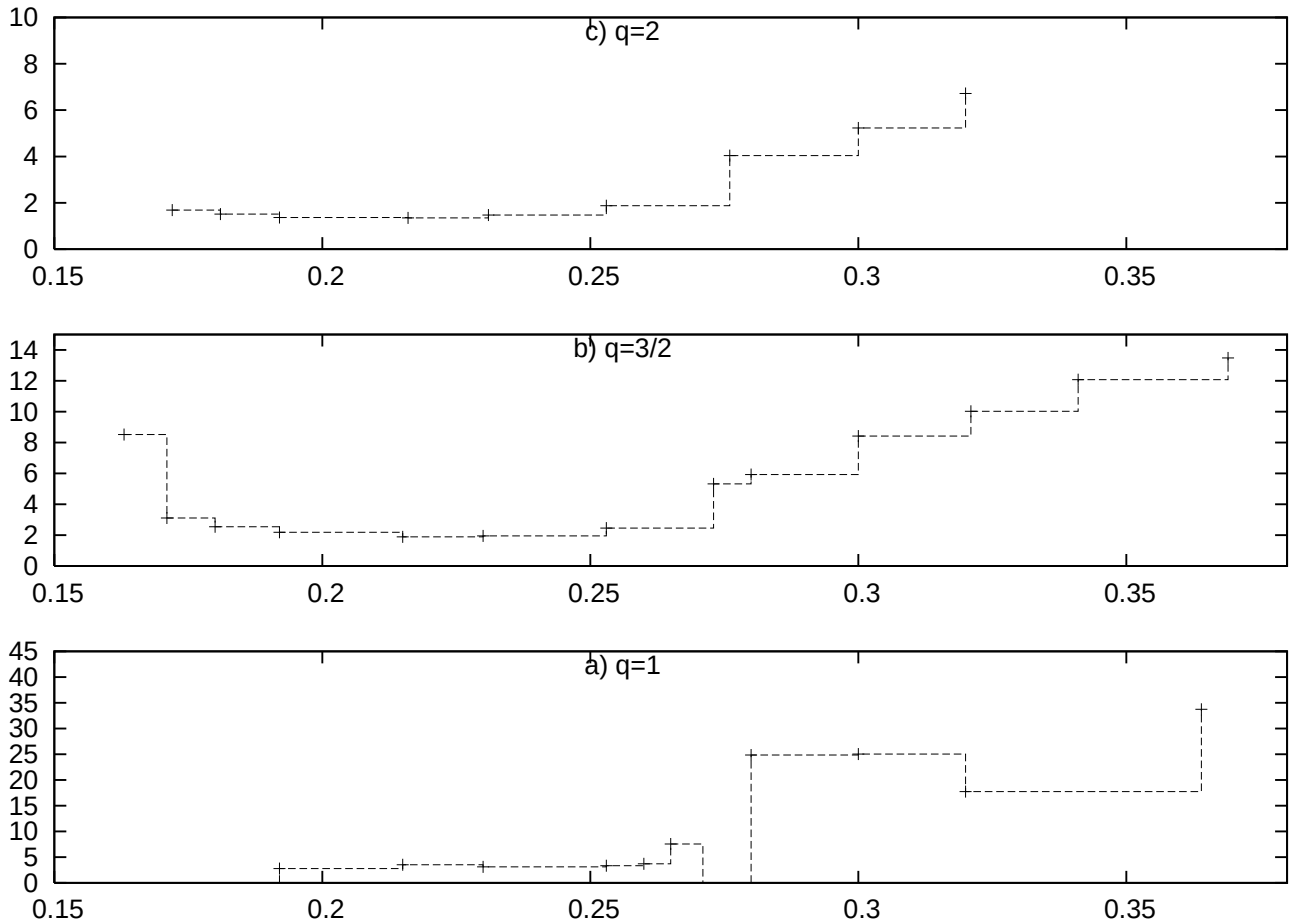

Fig. 8.— The ratio $\mathcal{R} = (\int \sigma_\Phi d^3x)/(\int \sigma_R d^3x)$ for the $m = 2$ mode for the $(n, q) = (3/2{,}3/2)$ toroid sequence.

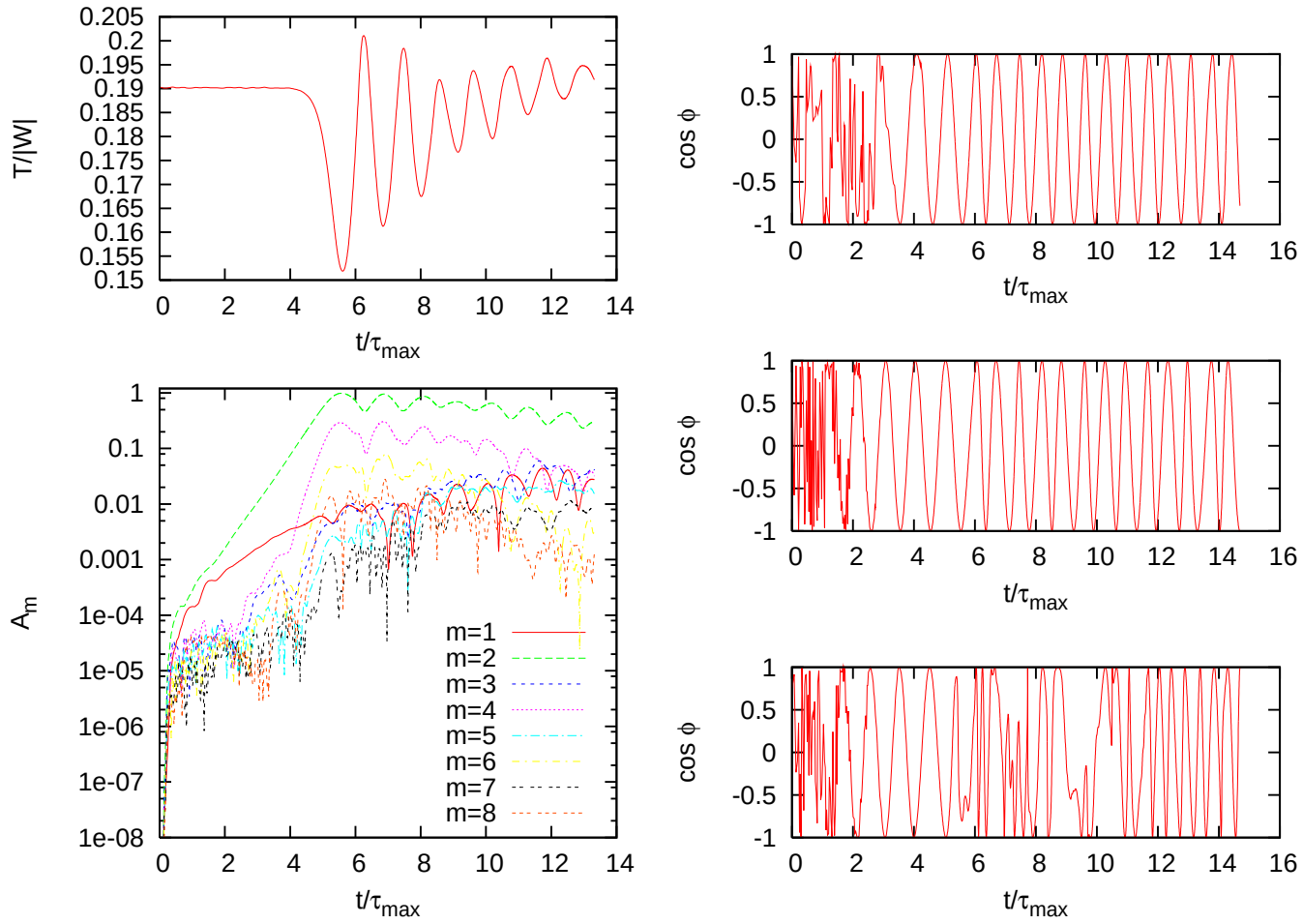

Fig. 9.— The $\mathcal{A}_m$ for $m = 1$ to 8, $T/|W|$, and $\cos(\phi_\rho)$ for the radii in the equatorial plane for the $(n, q) = (3/2,3/2)$, $T/|W| = 0.19$ toroid. (See $d131 - 29.uoregon.edu$: $/home/imamura/imamura/mickey/acad_cluster/shibata/nonlinear/t8$)

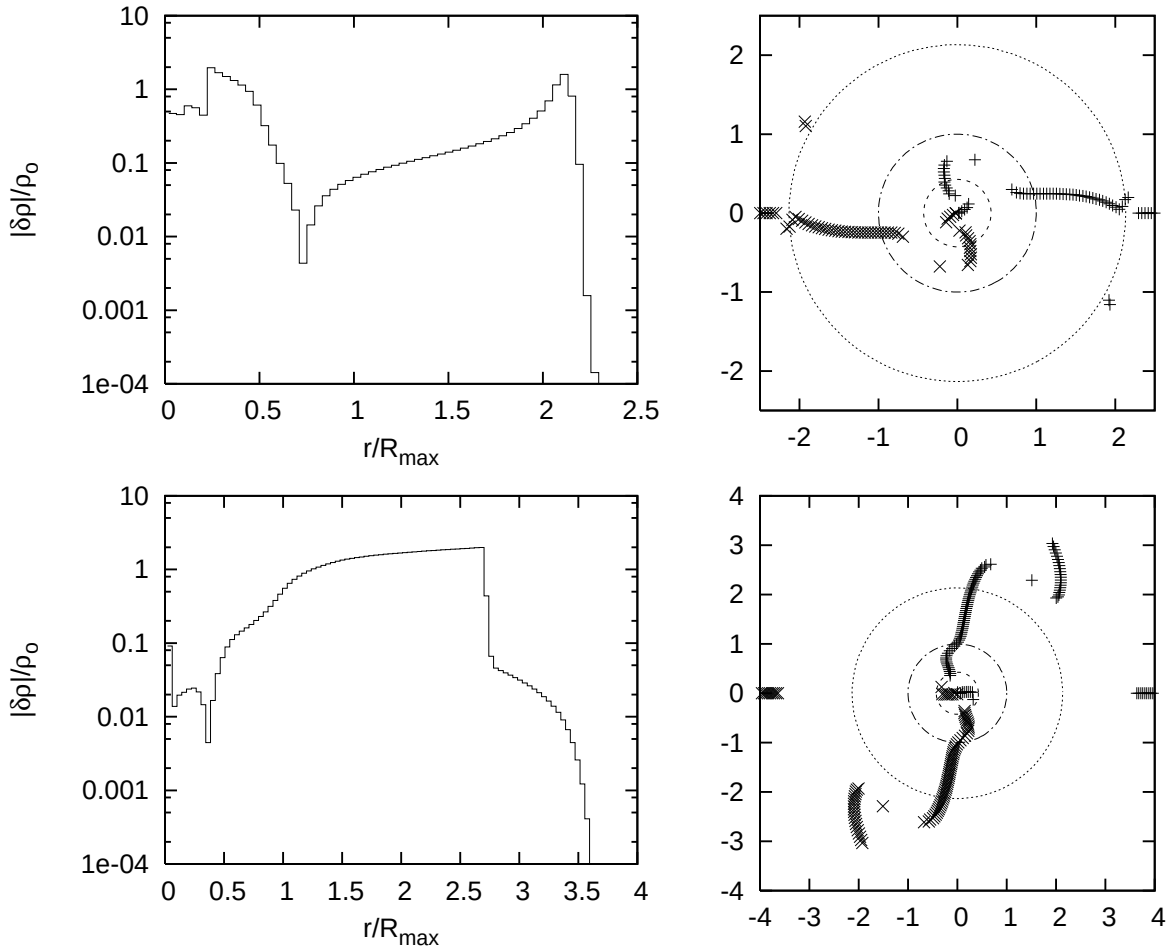

Fig. 10.— The $m = 2$ eigenfunction $|\delta\rho|$ in the equatorial plane of the $(n, q) = (3/2,3/2)$, $T/|W| = 0.192$ toroid at $t = 4.12\ \tau_{max}$ when $\mathcal{A}_2 = 0.098$, and $t = 5.54\ \tau_{max}$ when $\mathcal{A}_2 = 0.985$. In the phase plots (the right hand panel), the circles mark the inner edge, the location of density maximum, and the outer edge of the equilibrium toroid. (See $d131 - 29.uoregon.edu$: $/home/imamura/imamura/mickey/acad_cluster/shibata/nonlinear/t2$)

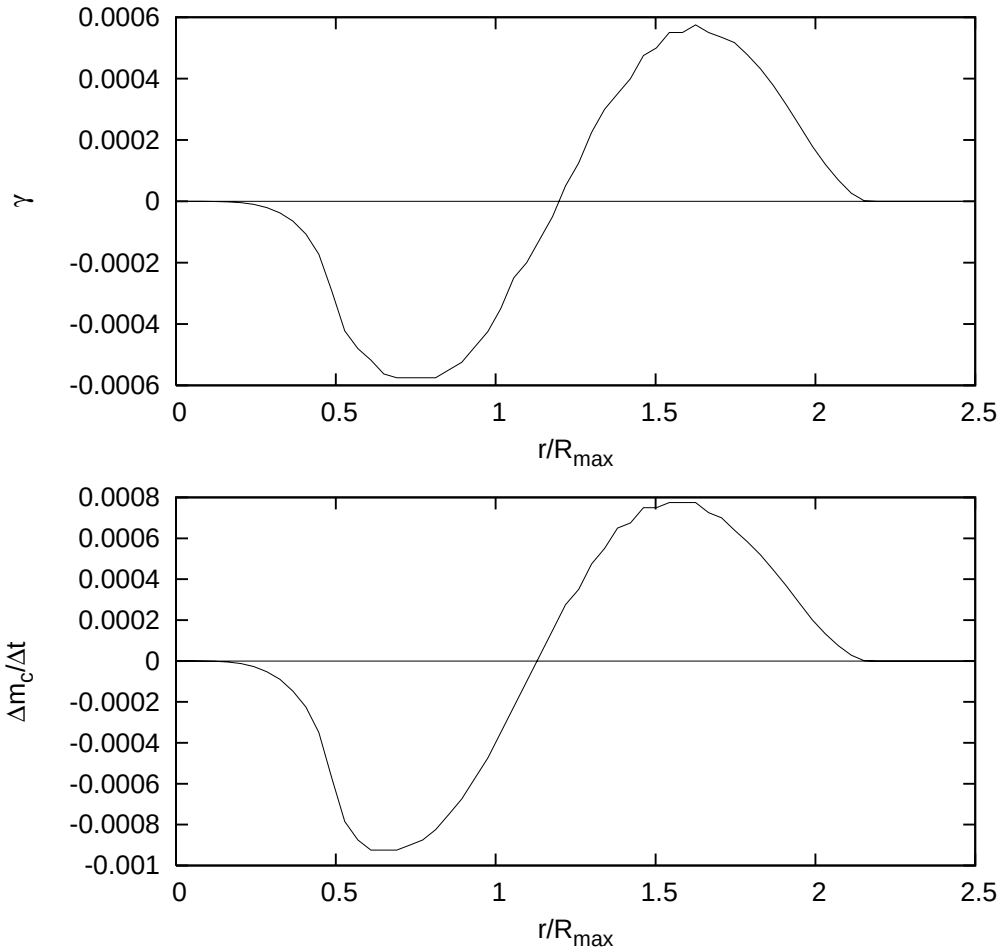

Fig. 11.— The $m = 2$ self-gravitational torque, γ_{nl} and $\dot{M} = \Delta m_c/\Delta t$ for the nonlinear simulation at $t = 4.54\ \tau_{max}$ when $\mathcal{A}_2 = 0.23$. At this time the $m = 2$ oscillation is near minimum (see Figure 9). Note the strong similarity in shape of the nonlinear torque to the quasi-linear self-gravitational torque shown in Figure 4. Quantitatively, there are differences. The angular momentum loss rate for the inner region of the toroid in the nonlinear simulation is roughly $\gamma_{nl} = -3.95 \times 10^{-3}$. The QL torque for $\mathcal{A}_2 = 0.23$ is $\gamma \sim -2.2 \times 10^{-3}$.

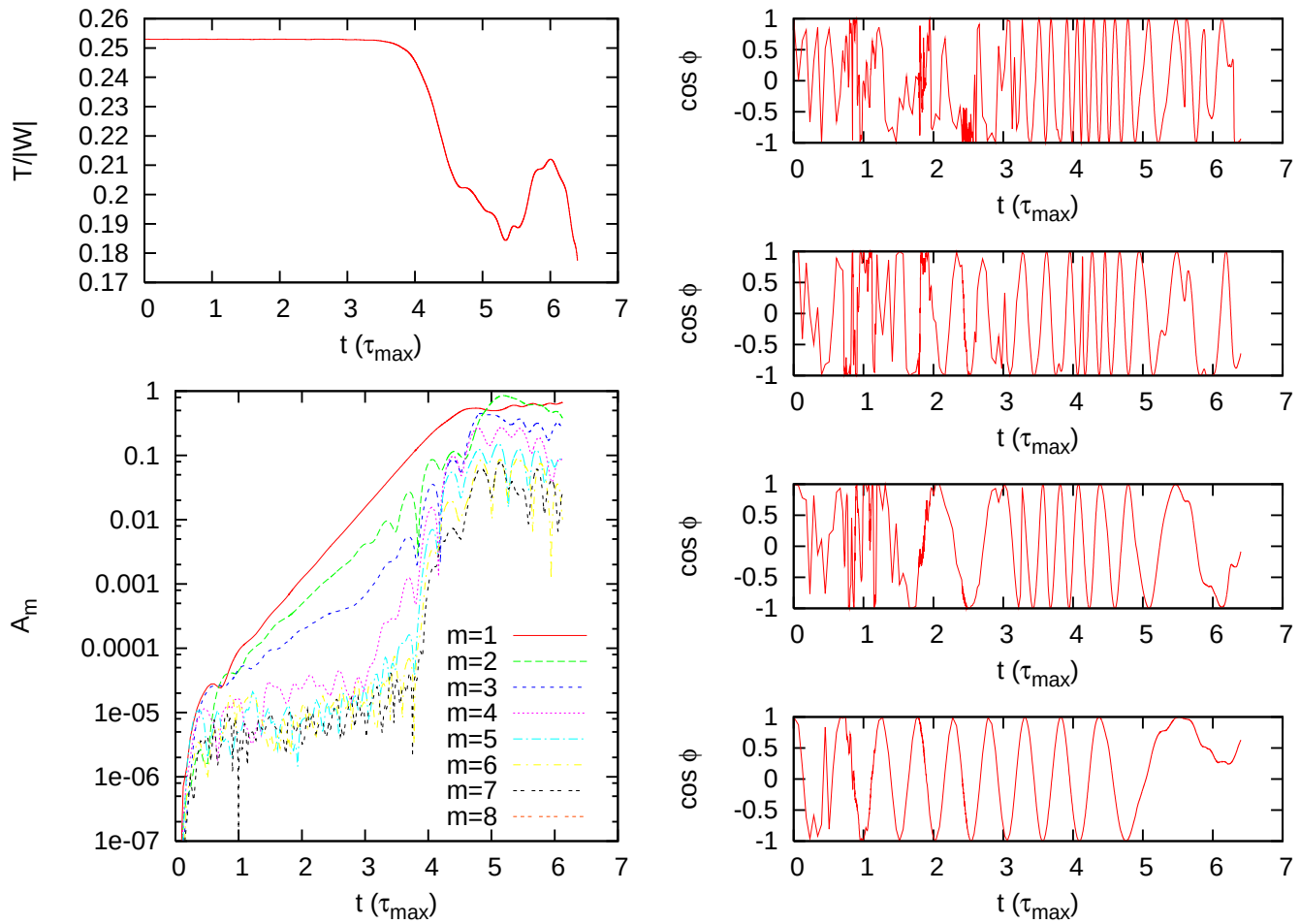

Fig. 12.— The $\mathcal{A}_m$, $T/|W|$, and $\cos(\phi_\rho)$ for the m = 1, 2, 3, and 4 modes (from bottom-to-top) for the (n, q) = (3/2,3/2) $T/|W|$ = 0.253 toroid.

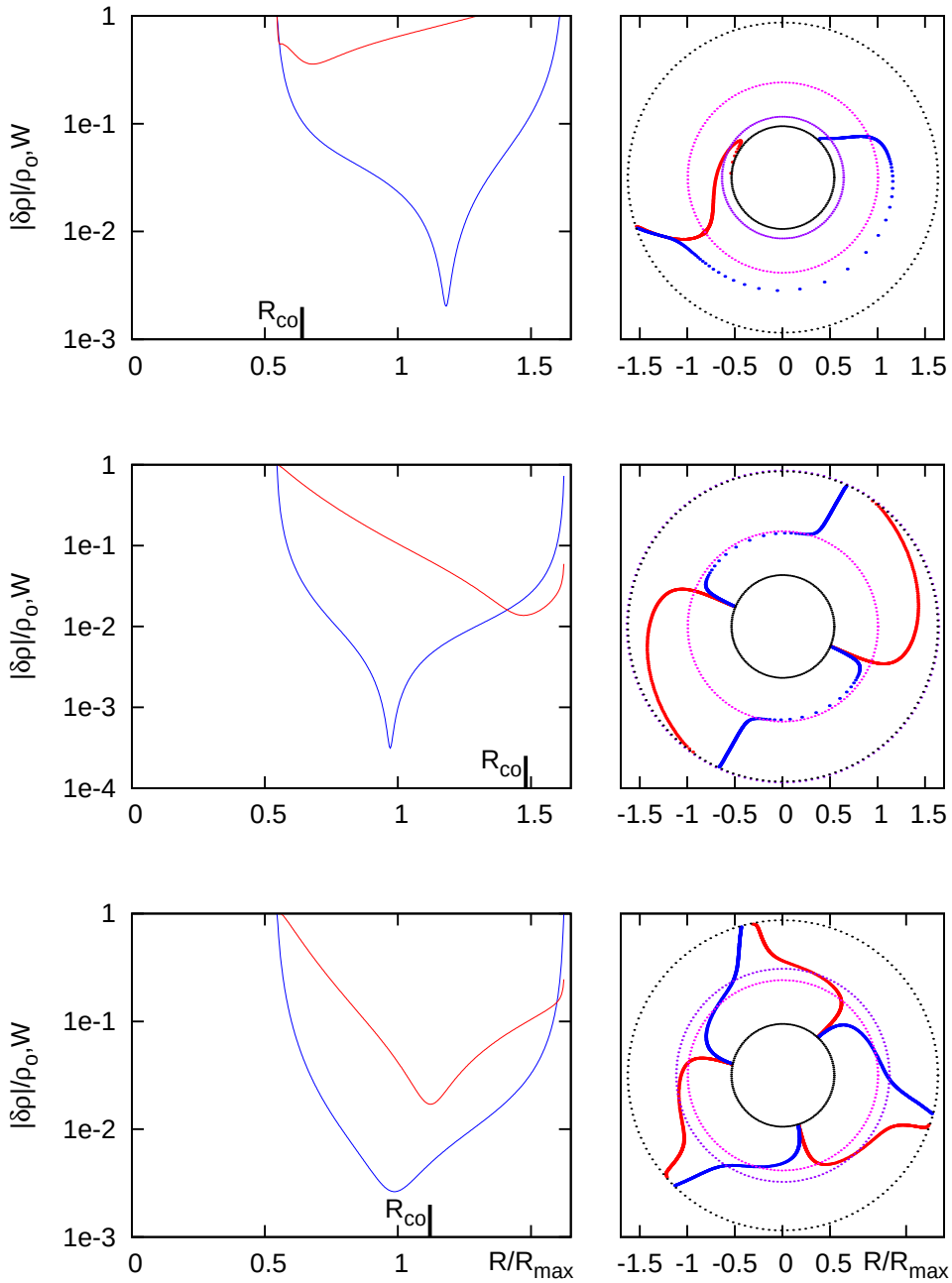

Fig. 13.— The $m = 1$, 2, and 3 mode eigenfunctions for the $(n, q) = (3/2{,}3/2)$, $T/|W| = 0.253$ toroid. The eigenfunctions and constant phase loci in the equatorial plane are shown. In the left hand panel, the solid line is $|\delta\rho|/\rho_\circ$ and the dashed line is $\mathcal{W}$. The three circles in the phase plot (right hand panel) mark the inner and outer radii of the toroid and the location of ρ_{max}.

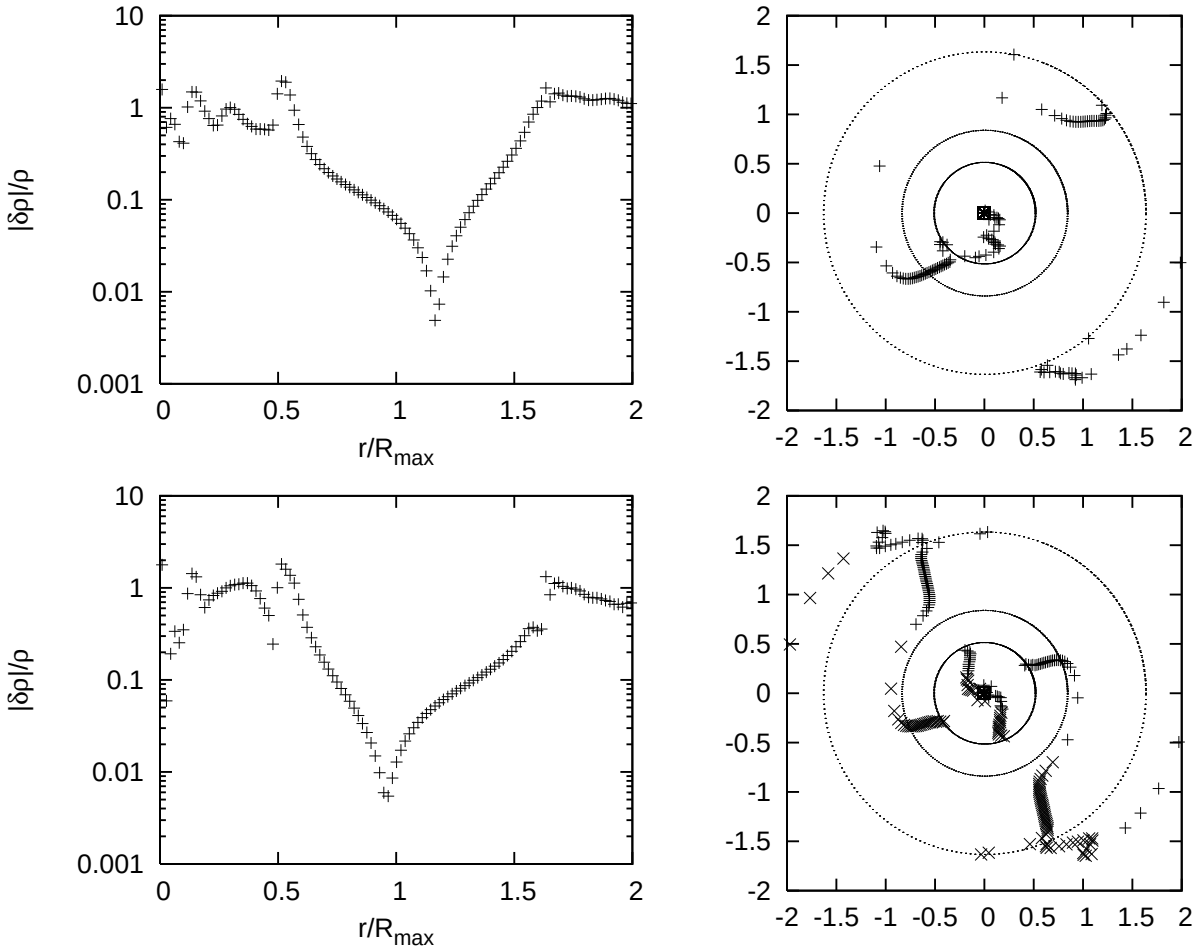

Fig. 14.— $m = 1$ and 2 relative density eigenfunctions in the equatorial plane for the $(n, q) = (3/2,3/2)$ toroid with $T/|W| = 0.253$ at time $t = 3.3\ \tau_{max}$. The inner and outer circles in the phase plots show the inner and outer edges of the equilibrium toroid and the interior circle shows the location of the maximum density ρ_{max} for the equilibrium toroid. (See $acad_cl3.uoregon.edu$: $/home3/imamura/disk/nonlinear/t9a$).

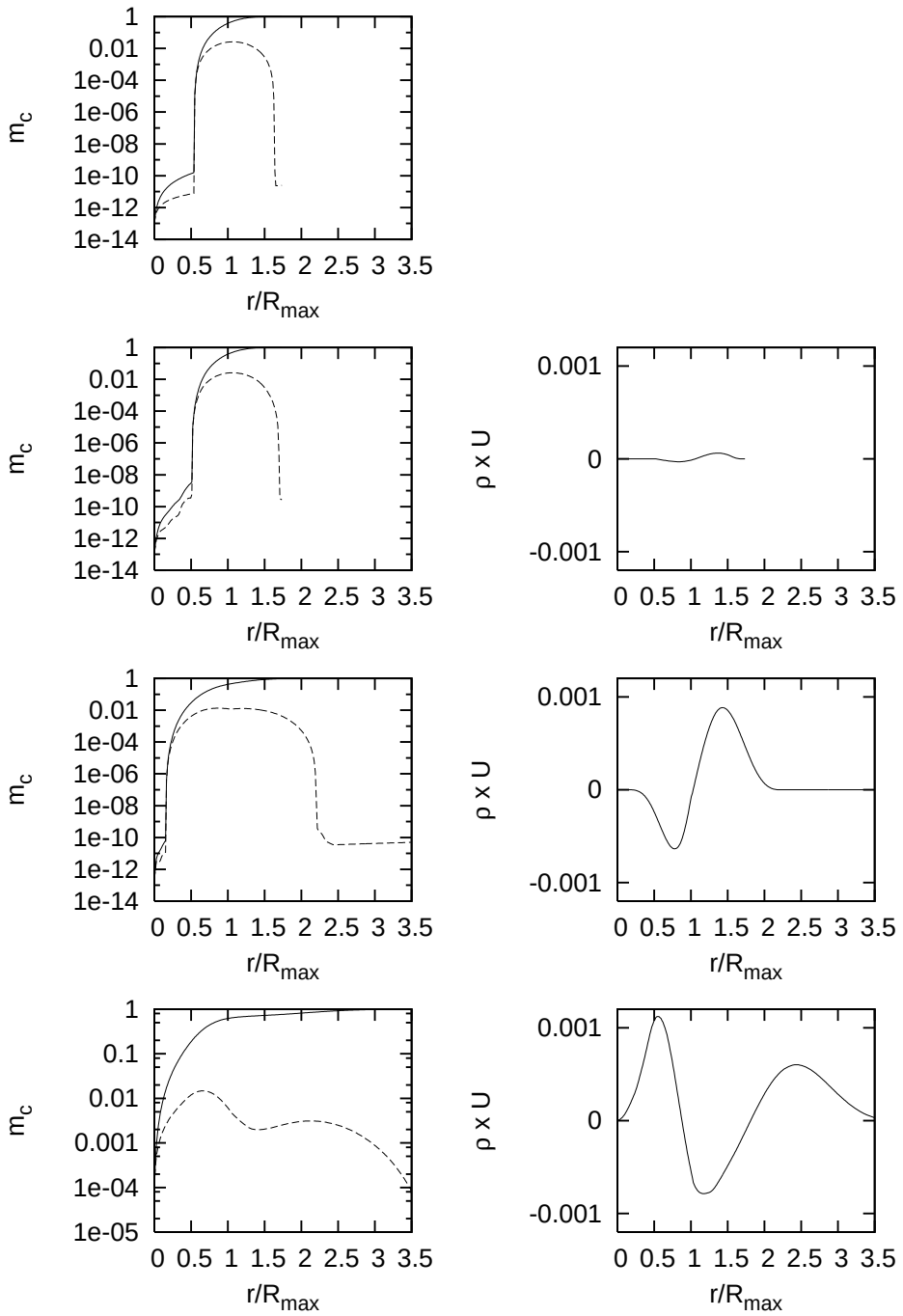

Fig. 15.— Left Panels: The cylindrical mass m_c and cylindrical mass distribution for the $(n, q) = (3/2,3/2)$ toroid with $T/|W| = 0.253$. In the plots, the upper curve, "+", is the integrated cylindrical mass and the lower curve "×", is the mass contained within an annulus of size $(\varpi, \varpi + \Delta\varpi)$. Right Panels: The mass fluxes $\rho \times U$, where U is the radial velocity, are shown for each of the mass distributions shown in the left hand panels. The mass distributions are shown at the times $t = 0$, 3.41 τ_{max}, 4.29 τ_{max}, 4.98 τ_{max} from top-to-bottom. (See $/home/imamura/imamura/mickey/DISK2/torus3d/t253_1$.)

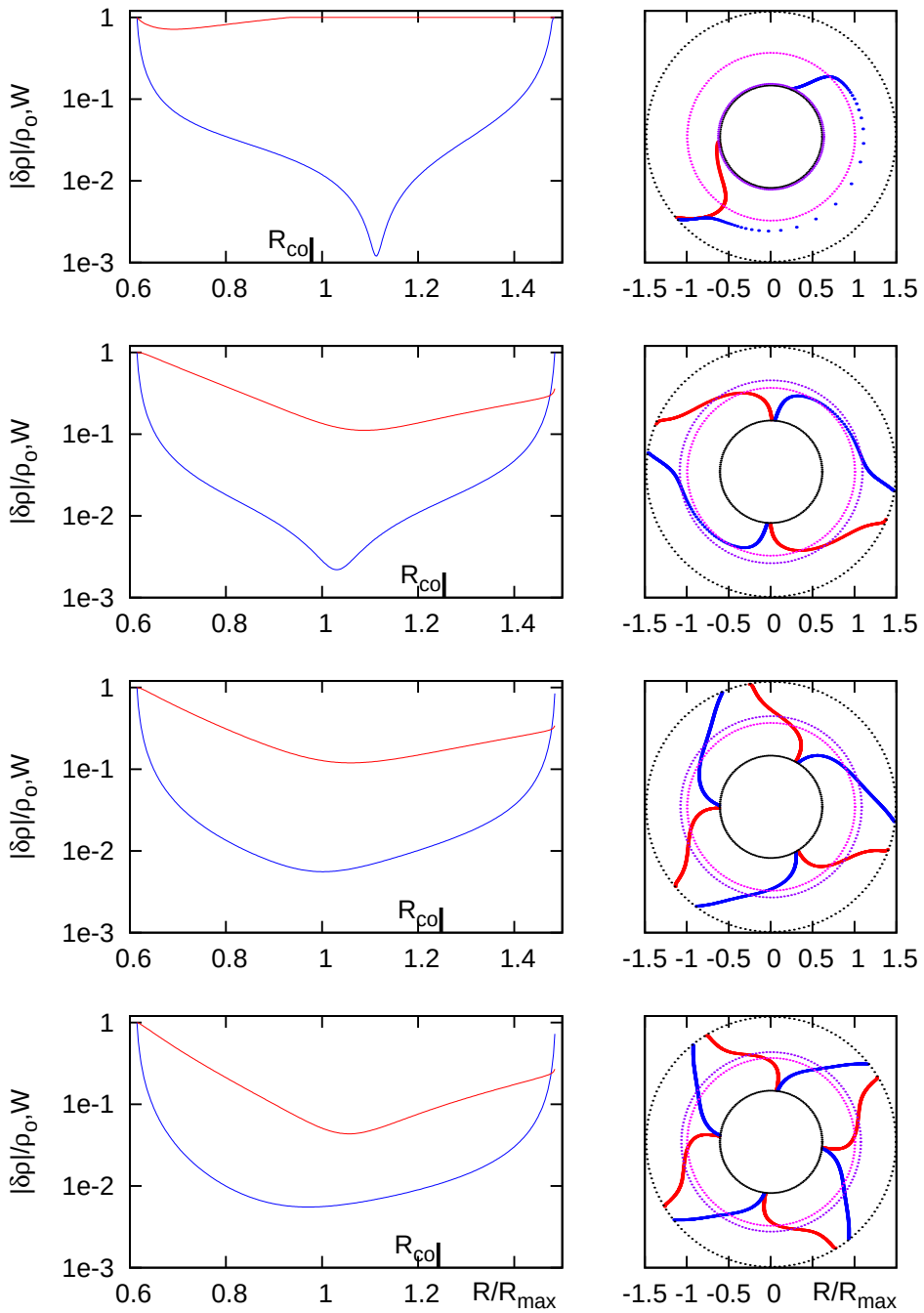

Fig. 16.— The m = 1, 2, 3, and 4 mode eigenfunctions for the (n, q) = (3/2,3/2), $T/|W|$ = 0.273 toroid. The eigenfunctions and constant phase loci in the equatorial plane are shown. In the left hand panel, the solid line is $|\delta\rho|/\rho_\circ$ and the dashed line is $\mathcal{W}$. The three circles in the phase plot (right hand panel) mark the inner and outer radii of the toroid and the location of ρ_{max}.

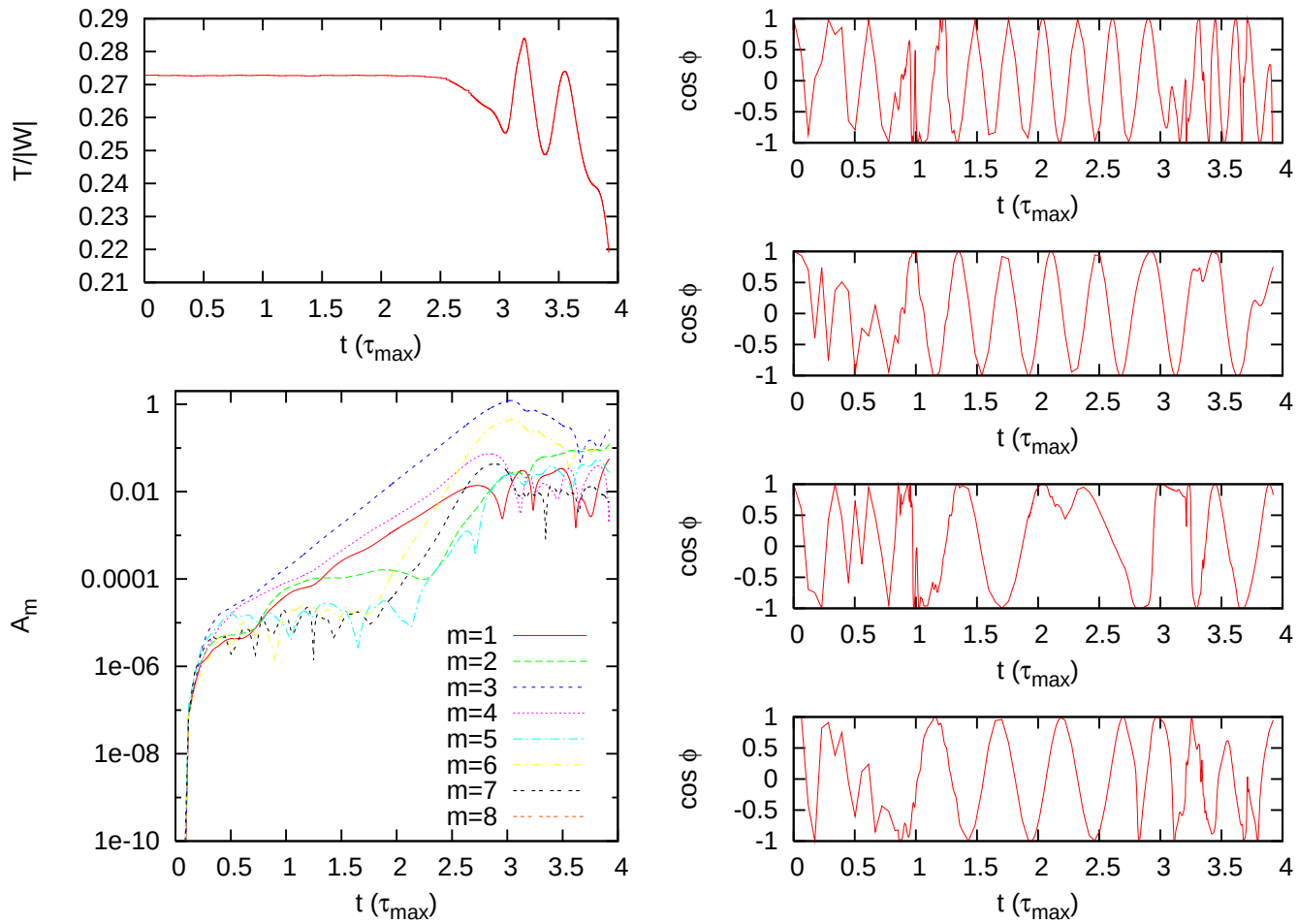

Fig. 17.— The $\mathcal{A}_m$, $T/|W|$, and $\cos(\phi_\rho)$ for the m = 1, 2, 3, and 4 modes (from bottom-to-top) for the (n, q) = (3/2,3/2) $T/|W|$ = 0.273 toroid. The phases are found for radius $r/R_+ = 0.67$.

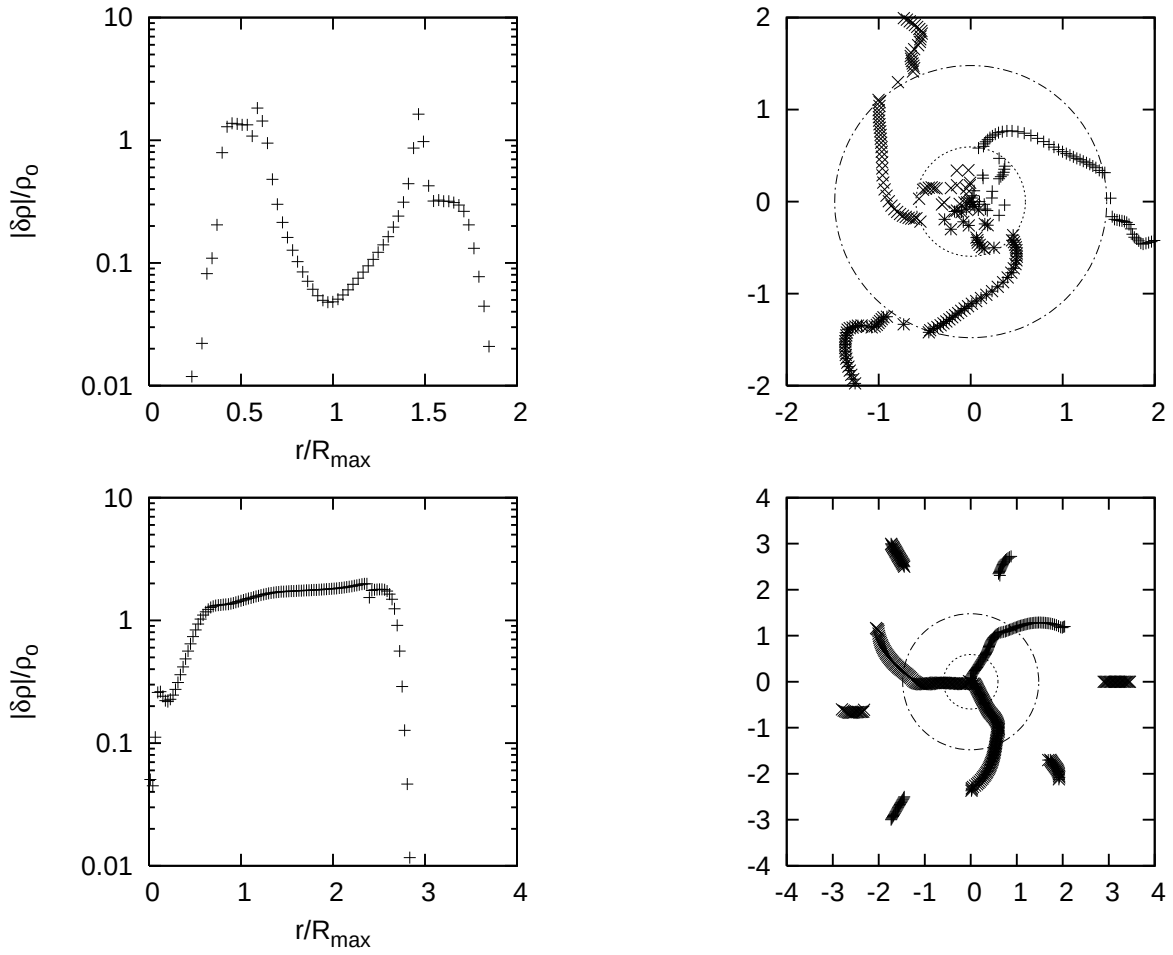

Fig. 18.— The $m = 3$ eigenfunction $|\delta\rho|/\rho_\circ$ and the constant phase locus for $\delta\rho$ in the equatorial plane for the $(n, q) = (3/2{,}3/2)$, $T/|W| = 0.272$ toroid at times $t = 1.98\ \tau_{max}$ and $2.84\ \tau_{max}$. The inner and outer circles in the phase plot mark the inner and outer edges of the equilibrium toroid. $(d131 - 29 : /home/imamura/imamura/mickey/acad_cluster/disk/nonlinear/t1)$

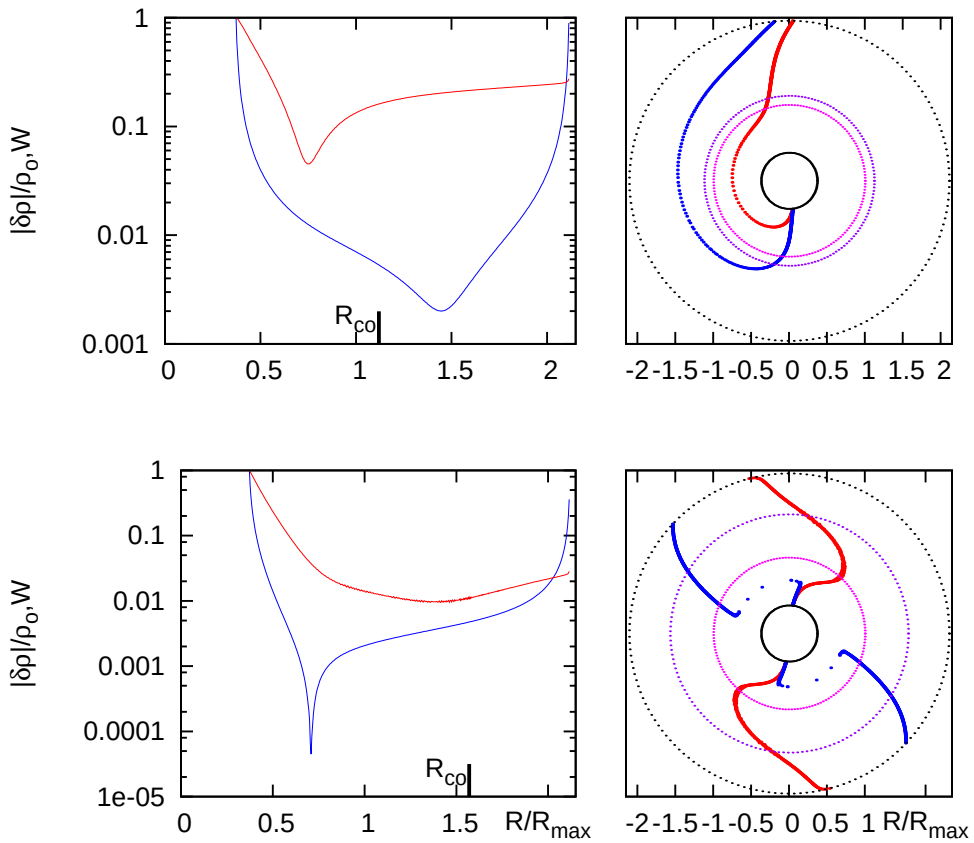

Fig. 19.— The $m = 1$ and 2 eigenfunctions for the star/disk system with $M_*/M_d = 0.05$ and disk with $(n, q) = (3/2{,}3/2)$, $T/|W| = 0.219$ toroid.

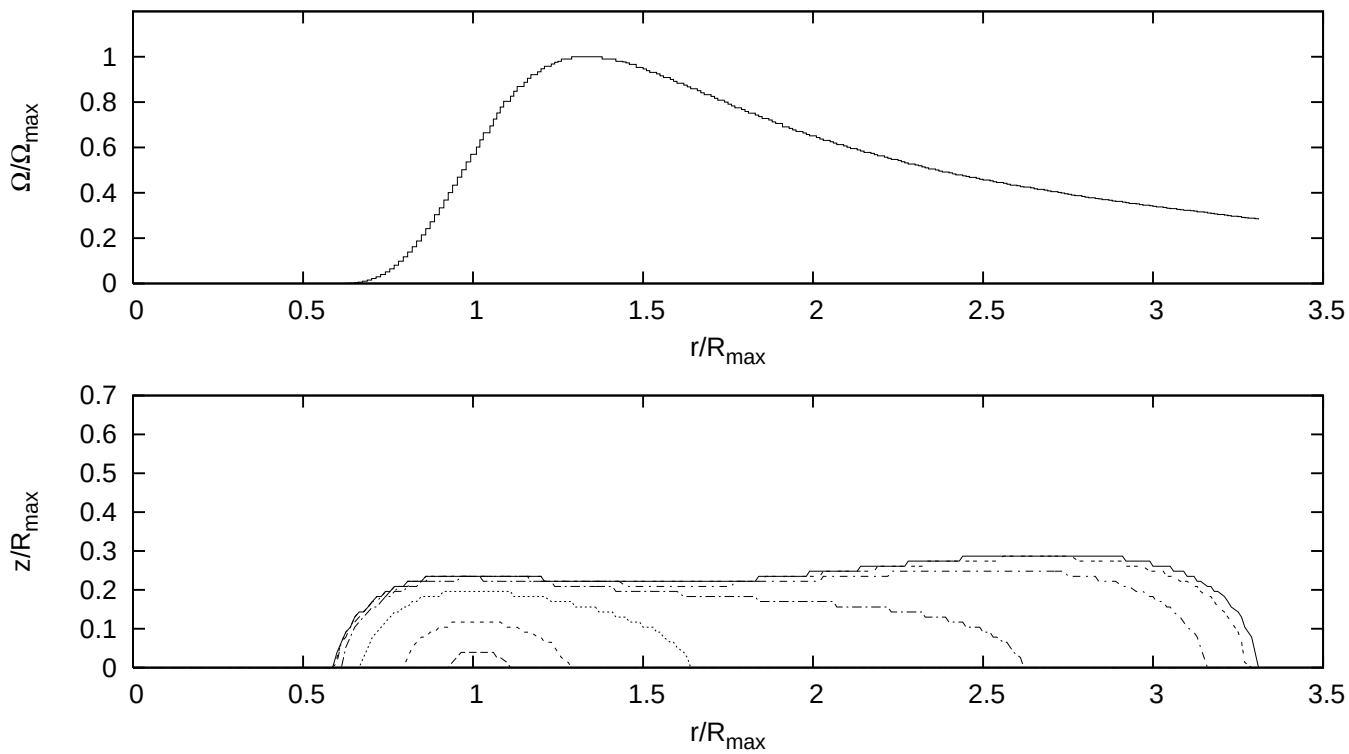

Fig. 20.— The equilibrium structure for a Maclaurin-like toroid with $R_-/R_+ = 0.178$, $j = 2.90$, and $T/|W| = 0.384$. The top panel shows the angular velocity distribution and the bottom panel shows density contours in a meridional slice. The contours in density are placed at levels of ρ/ρ_{max} = 0.9, 0.5, 0.1, 0.01, 0.001, and 10^{-7}. The lengths are normalized using $R_{max} = 15.1$ and the angular velocities by $\Omega_{max} = 0.0102$.

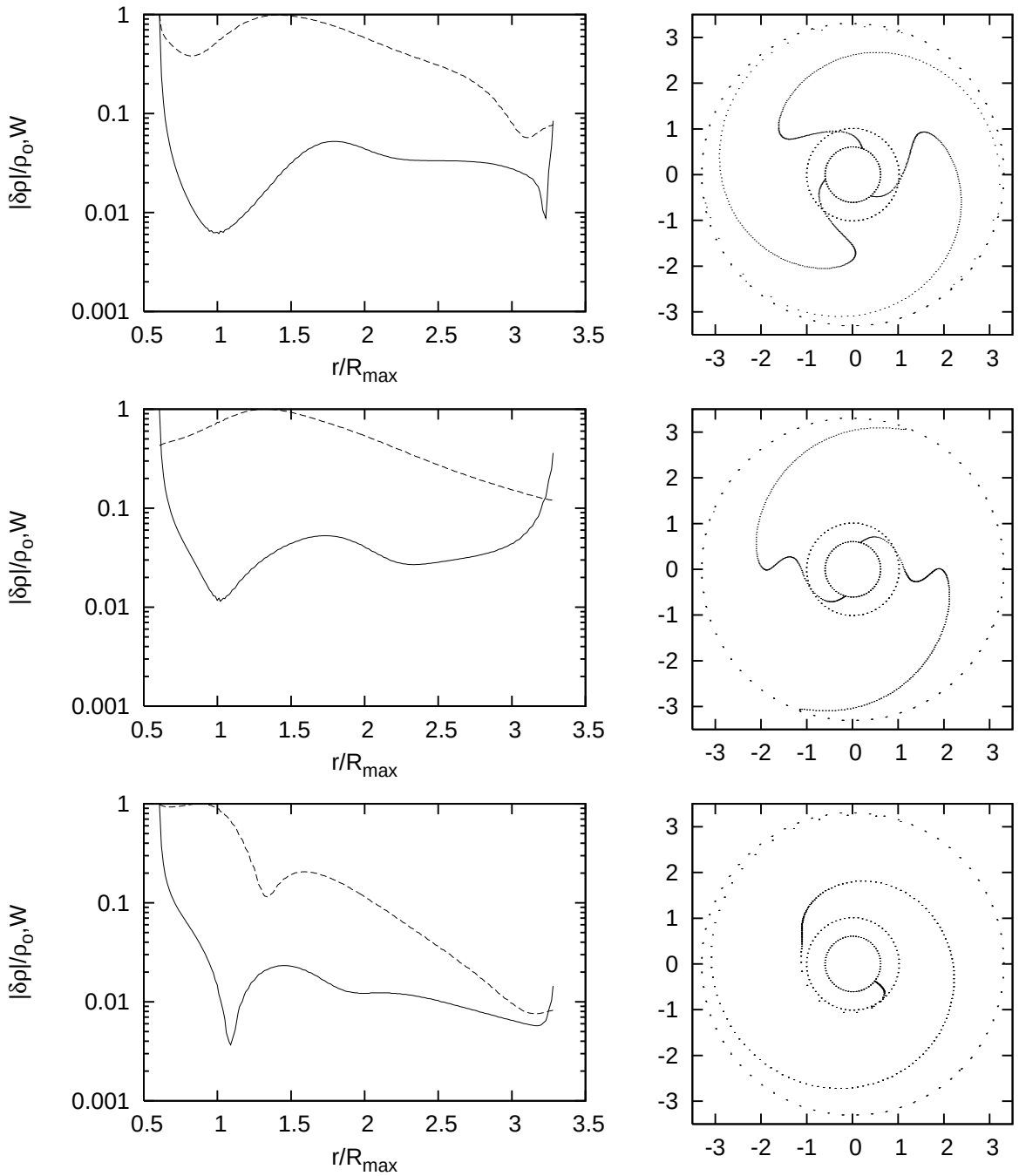

Fig. 21.— The $m = 1$, 2, and 3 density eigenfunctions for the Maclaurin-like toroid with $R_-/R_+ = 0.178$, $j = 2.90$, and $T/|W| = 0.384$. The eigenfunctions are for the $m = 1$, 2, and 3 modes from bottom-to-top. The lengths are normalized in units of $R_{max} = 15.1$.